

2016-01-01

Design and Performance Evaluations of a LO2/ Methane Reaction Control Engine

Aaron Johnson

University of Texas at El Paso, ajohnson2033@gmail.com

Follow this and additional works at: https://digitalcommons.utep.edu/open_etd



Part of the [Aerospace Engineering Commons](#), and the [Mechanical Engineering Commons](#)

Recommended Citation

Johnson, Aaron, "Design and Performance Evaluations of a LO2/Methane Reaction Control Engine" (2016). *Open Access Theses & Dissertations*. 671.

https://digitalcommons.utep.edu/open_etd/671

This is brought to you for free and open access by DigitalCommons@UTEP. It has been accepted for inclusion in Open Access Theses & Dissertations by an authorized administrator of DigitalCommons@UTEP. For more information, please contact lweber@utep.edu.

DESIGN AND PERFORMANCE EVALUATIONS OF A LO₂/METHANE
REACTION CONTROL ENGINE

AARON JOHNSON

Master's Program in Mechanical Engineering

APPROVED:

Ahsan Choudhuri, Ph.D., Chair

Norman Love Jr., Ph.D.

Tzu-Liang (Bill) Tseng, Ph.D., CMfgE

Charles Ambler, Ph.D.
Dean of the Graduate School

Copyright ©

by

Aaron Johnson

2016

Dedication

I would like to dedicate this thesis to my family and friends all of whom have supported me unconditionally in this crazy journey through life. CS.

DESIGN AND PERFORMANCE EVALUATIONS OF A LO₂/METHANE
REACTION CONTROL ENGINE

by

AARON JOHNSON, B.S. Mechanical Engineering

THESIS

Presented to the Faculty of the Graduate School of

The University of Texas at El Paso

in Partial Fulfillment

of the Requirements

for the Degree of

MASTER OF SCIENCE

Department of Mechanical Engineering

THE UNIVERSITY OF TEXAS AT EL PASO

December 2016

Acknowledgements

I would like to thank Dr. Ahsan Choudhuri for giving me the opportunity to grow as an engineer and as a person, by allowing me to participate in research at UTEP. I would also like to thank NASA for their mentorship along the way and their belief in the students at cSETR. A special thanks to my committee as well, Dr. Norman Love and Dr. Bill Tseng for giving their time to review my research.

I would definitely like to acknowledge a mentor of mine, Mr. Charles Hill, who consistently made sure I was on top of things with my project (even though we always ended right back at the requirements phase).

A very special thanks needs to go out to my team both past and present who made all of this possible by their hard work and efforts: Arturo Acosta-Zamora, Jose Luis Mena, Israel Lopez, Raul Ponce, Pedro Nunez, Dylan Ott, and Steven Torres. I am eternally grateful for the time they put into the project and will never forget the sacrifices (long hour weeks/weekends) that were made along the way.

I would also like to acknowledge my parents, Jack and Lucy Johnson, my sister, Amanda Johnson, and my girlfriend, Thania Cervantes, for consistently being there to support me. I love you all.

Thank you as well to the cSETR staff; specifically, Gloria Salas and KiraLise Silva for consistently putting up with my purchase requests and never getting annoyed with me along the way.

Lastly, thank you to all of the casita folks both past and present for making this an incredible ride and journey.

Abstract

Liquid oxygen (LOX) and liquid methane (LCH₄) are a propellant combination viewed as a potential enabling technology for spacecraft propulsion. Reasons why LOX/LCH₄ is being used as an alternative propellant source include: it is less toxic than other propellants, it has the possibility to be harvested on extraterrestrial soil, LCH₄ has a higher energy density than liquid hydrogen (LH₂; commonly used on vehicle main engines), and LOX/LCH₄ has comparable performance to other well-known propellant combinations. Through the continued partnership between the National Aeronautics and Space Administration (NASA) and the University of Texas at El Paso (UTEP) a LOX/LCH₄ reaction control engine (RCE) was developed and researched. The RCE was developed for the purpose of being integrated into two UTEP LOX/LCH₄ vehicles, Janus and Daedalus, and was designed based on previous engines tested both at NASA and the center for space exploration and technology research (cSETR) lab. This report details the design process and manufacturing of the engine, cold flow studies evaluating injector design, and preliminary hot fire tests to give insight into engine performance.

Table of Contents

Acknowledgements.....	v
Abstract.....	vi
List of Tables.....	ix
List of Figures.....	x
Chapter 1: Introduction.....	1
Chapter 2: Reaction Control Engine Background.....	3
Chapter 3: RCE Development Purpose.....	5
3.1 Janus and Daedalus Vehicle Overview.....	5
3.2 Vehicle Flight Profiles.....	7
3.3 Vehicle Development.....	9
Chapter 4: RCE Design Requirements.....	10
Chapter 5: RCE Component Design.....	15
5.1 Nozzle and Chamber Design.....	15
5.2 Injector Design.....	17
5.3 Ignition Method.....	19
5.4 RCE Assembly for Testing and Flight.....	21
Chapter 6: Manufactured Reaction Control Engine.....	24
6.1 Chamber and Injection Orifices.....	24
6.2 Nozzle.....	25
6.3 Spark Plug with Extended Electrode.....	26
6.4 Inspection on Machined Parts.....	27
6.5 Welded Engine Assembly.....	27
Chapter 7: Cold Flow Testing.....	29
7.1 Water Test Set Up.....	29
7.2 Data Acquisition.....	31
7.3 Test Results.....	32
7.4 FFC Testing and Validation.....	36

Chapter 8: Preliminary Hot Fire Testing.....	38
8.1 Test Bunker Facility.....	38
8.2 DAQ and Instrumentation Controller.....	42
8.3 Hot Fire Test Results.....	44
8.3.1 Gas/Gas Testing.....	44
8.3.2 Liquid/Liquid Testing.....	50
Chapter 9: Future Work and Conclusions.....	56
9.1 Proposed Hot Fire Test Matrix.....	56
9.2 Potential Incorporation of Additive Manufacturing.....	57
9.3 Overall Conclusions.....	61
Bibliography.....	62
Appendix:.....	64
Vita.....	74

-

List of Tables

Table 4.1: Top Level RCE Requirements.....	14
Table 6.1: Inspection of key features within RCE.....	27
Table 7.1: Water test results for both the LOX and LCH4 lines.	33
Table 7.2: Test results for FFC cold flow studies.....	37
Table 8.1: Hot fire test results for gas/gas testing.....	45
Table 8.2: Hot fire test results for liquid/liquid testing.....	50
Table 8.3: Engine performance results for liquid/liquid testing.	50
Table 8.4: Uncertainty analysis on thrust stand measurement.....	51
Table 8.5: Predicted chamber pressures based on RPA software.....	54
Table 9.1: Proposed test matrix for liquid/liquid testing.	56
Table 9.2: Test matrix and results of water testing the LOX injection ports.....	59

List of Figures

Figure 2.1: Motivation behind RCS thruster, NASA's project Morpheus vehicle.....	3
Figure 2.2: RCS Thruster Assembly and Components.....	4
Figure 3.1: Conceptual Design of Vertical Test Bed, Janus.....	6
Figure 3.2: Conceptual Design of Suborbital Test Bed, Daedalus	7
Figure 3.3: Janus Flight Profile.....	7
Figure 3.4: Daedalus Flight Profile.....	8
Figure 4.1: Specific Impulse vs Expansion Ratio at varying mixture ratios, $P_c = 100$ psi.....	11
Figure 4.2: Chamber Temperature vs Chamber Pressure at varying mixture ratios.....	12
Figure 4.3: Specific Impulse vs Mixture Ratio for Janus & Daedalus engines.....	13
Figure 5.1: Cross sectional view of nozzles for both Janus (nozzle A) and Daedalus (nozzle B) RCEs.....	16
Figure 5.2: Cross sectional view of the chamber showing regions which would be cut to reduce chamber length and further study L^* effects.....	17
Figure 5.3: Cross sectional view of the RCE detailing injection inlets.....	18
Figure 5.4: Cross sectional view of the RCE injection manifolds for LOX (left) and LCH ₄ (right).....	18
Figure 5.5: Spark plug to machined electrode interface and weld location.....	20
Figure 5.6: Potential arc location (yellow indicator) of the spark electrode to the thrust chamber.....	20
Figure 5.7: RCE assembly to be fabricated for test purposes.....	21
Figure 5.8: Cross sectional view of the RCE assembly for test purposes.....	21
Figure 5.9: Flight design for the RCE to be integrated within the Daedalus vehicle.....	22
Figure 5.10: Cross sectional view of the flight RCE to be used in the Daedalus vehicle.....	23
Figure 6.1: Various views of the machined RCE chamber without the injection orifices.....	24

Figure 6.2: RCE chamber with injection orifices machined onto to it.	25
Figure 6.3: RCE nozzle side view (left) and top view (right).....	25
Figure 6.4: RCE ignition source; modified spark plug with extended electrode tip.....	26
Figure 6.5: Final manufactured and welded RCE assembly.....	28
Figure 7.1: Water test piping and instrumentation diagram (P&ID).	29
Figure 7.2: Full view of the water test set up from the tank to the RCE.	30
Figure 7.3: Components and instrumentation within the water test set-up.....	30
Figure 7.4: Block diagram of the flowmeter logic.....	31
Figure 7.5: Block diagram of the pressure transducer and thermocouple logic.	32
Figure 7.6: Correlation between discharge coefficient and Reynolds number.	34
Figure 7.7: Predicted LOX flowrates based on predicted and measured Cd values.....	35
Figure 7.8: Predicted LCH4 flowrates based on predicted and measured Cd values.	36
Figure 8.1: cSETR propulsion lab test bunker layout.....	38
Figure 8.2: LOX feed line to the MASS.....	39
Figure 8.3: Methane condensing unit and LCH4 feed lines.	39
Figure 8.4: Instrumentation and set-up within the MASS.....	40
Figure 8.5: Close up of the RCE on the torsional thrust stand.	41
Figure 8.6: Highlighted components within the MASS.....	41
Figure 8.7: TTS calibration data used for thrust measurement.....	42
Figure 8.8: Front panel LabVIEW GUI for liquid/liquid testing.....	42
Figure 8.9: Automated sequence loaded into the LabVIEW controller.....	43
Figure 8.10: Automated sequence block diagram.....	43
Figure 8.11: Solenoid valve control structure block diagram.....	44

Figure 8.12: Thermocouple locations on the engine chamber and nozzle.....	45
Figure 8.13: Gas/gas hot fire test results for $MR=1.83$	46
Figure 8.14: Gas/gas hot fire test results for $MR=1.93$	47
Figure 8.15: Gas/gas hot fire test results for $MR=2.26$	48
Figure 8.16: Gas/gas hot fire test chamber pressure results.....	49
Figure 8.17: Video imaging of the gas/gas tests; A) $MR=2.26$, B) $MR=1.93$, C) $MR=1.83$	49
Figure 8.18: Liquid/liquid hot fire test results for $MR=0.35$	51
Figure 8.19: Liquid/liquid hot fire test results for $MR=0.81$	52
Figure 8.20: Liquid/liquid hot fire test results for $MR=1.15$	53
Figure 8.21: Liquid/liquid hot fire tests chamber pressure results.....	54
Figure 8.22: Video imaging of the liquid/liquid tests; A) $MR=0.35$, B) $MR=0.81$, C) $MR=1.15$	55
Figure 9.1: SLM manufacturing process, starting from the top right.	58
Figure 9.2: Post machined 3D printed engine.....	58
Figure 9.3: Nozzle view (A) and the igniter view (B).	59
Figure 9.4: LOX line pressure drop vs mass flow rate correlation.	60

Chapter 1: Introduction

Liquid oxygen (LOX) and liquid methane (LCH₄) are a propellant combination viewed as a potential enabling technology for spacecraft propulsion. Some of the reasons why LOX/LCH₄ is being used as an alternative propellant source include: it is less toxic than other propellants, it has the possibility to be harvested on extraterrestrial soil, LCH₄ has a higher energy density than liquid hydrogen (LH₂; commonly used on vehicle main engines), and LOX/LCH₄ has comparable performance to other well-known propellant combinations.

One key reason for using LOX/LCH₄ is the potential for in-situ resource utilization (ISRU) or essentially the ability to harvest/process propellant on extraterrestrial soil. Having this ability allows for more payload to be carried on a spacecraft, instead of propellant, given that the propellant would be able to be “mined” within a planet such as Mars. With the National Aeronautics and Space Administration’s (NASA) current mission being the journey to Mars on the space launch system (SLS), LOX/LCH₄ can end up being an important part of spacecraft propulsion systems down the road due to its ISRU capabilities.

Under the following NASA grant number, NNX15AQ04A, the University of Texas at El Paso (UTEP) has had the privilege to continue research related to LOX/LCH₄ propulsion within the center for space exploration and technology research lab (cSETR). The research that will be discussed within this paper is with regards to a LOX/LCH₄ reaction control engine (RCE) and the performance derived from testing it at various parameters. The RCE is a derivative of previous work conducted both at NASA and cSETR and is designed around being integrated within two flight vehicles, Janus and Daedalus. Janus is a vertical test bed vehicle which will be tested in the El Paso region, while Daedalus is a suborbital test vehicle which will be launched as a payload to sub orbit. Both vehicles will incorporate propulsions systems that will demonstrate the feasibility of using a single LOX/LCH₄ propulsion system which will be used by both the main engine and the reaction control system.

The RCE discussed within this research was designed such that it would be able to vary fuel film cooling percentages and eventually be shortened with regards to chamber length; these two parameters play an important role in evaluating engine performance. The details documented within this report discuss the background of the RCE, the design requirements set for the engine, manufacturing of the RCE, and testing of the engine. Both cold flow and hot fire tests were conducted to evaluate both engine design and engine performance.

Chapter 2: Reaction Control Engine Background

The RCS thruster was developed and designed for NASA's project Morpheus vehicle which is shown below in figure 2.1¹



Figure 2.1 Motivation behind RCS thruster, NASA's project Morpheus vehicle

Morpheus is a vertical test bed vehicle which uses LOX/LNG as the main propellant source for both the main engine and the RCS engines. This type of vehicle is typically rare within spacecraft design because of the uncertainty associated with engine reliability and performance; specifically with the RCS. For that reason, some of the major questions that NASA wanted to address with regards to a LOX/LNG cryogenic RCS engine included: whether or not the engine would be able to provide repeatable pulses, how propellant quality for the engine would be maintained, and what type of ignition system would be used².

To keep the complexity of the engine to a minimum the RCS thruster was initially designed based on a converted torch igniter from an Aerojet engine³. After the initial phase of LOX/LNG performance testing a second RCS thruster was developed to be used specifically for the Morpheus vehicle. This specific thruster incorporated an integrated spark igniter, small fuel and oxidizer manifolds for low dribble volumes, and fast response solenoid valves which assembled directly onto the propellant manifolds. This type of design allowed for simplicity of the power system on the Morpheus vehicle, it was compact in size thus decreasing the amount of

¹ (Siceloff, 2014)

² (Hurlbert, Mcmanamen, Sooknanen, & Studak)

³ (Hurlbert, Romig, Collins, Allred, & Mahoney, 2010)

volume necessary, and was light with regards to weight. Figure 2.2 below gives a brief description of the engine and the associated components²

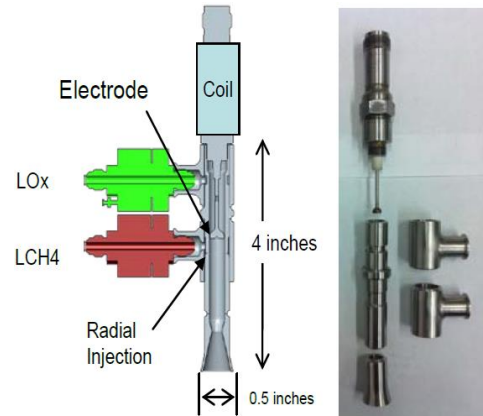


Figure 2.2 RCS thruster assembly and components

The RCE was then researched further by both NASA and cSETR and data was collected for various test firing conditions. However, what was seen by cSETR researchers was the engine was performing lower than expected. Thus, a test campaign was developed in which improvements to the facility and the engine design took place.

Chapter 3: RCE Development Purpose

The reaction control engine was designed to be implemented within two flight vehicles, Janus and Daedalus, and will be used for attitude control purposes and to perform vehicle maneuvers. This chapter will discuss in moderation the vehicle overviews, the flight profiles, and the development processes of Janus and Daedalus.

3.1 Janus and Daedalus Vehicle Overview

Janus is a robotic lander vehicle that serves as a methane propulsion technology testbed. The goal of Janus is to develop a flight-capable vehicle that incorporates various methane technologies into a fully operational autonomous (i.e. robotic) system⁴. These technologies include the use of a LOX/LCH₄ propulsion system and a methane solid oxide fuel cell (SOFC). Moreover, Janus will potentially demonstrate additive manufacturing for vehicle component design and implementation, as well as composite tank and vehicle structures. The propulsion system of Janus incorporates a gimbaled & throattleable 500-2000 lbf LOX/LCH₄ main engine and at least 4 5 lbf LOX/LCH₄ reaction control engines. The vehicle is a two tank vertical configuration that is half the size of NASA's Morpheus lander and uses a blowdown pressurization method which allows for the minimal number of tanks for operation. Figure 3.1 below shows the conceptual design and envelope of Janus

⁴ (Lopez, 2016)

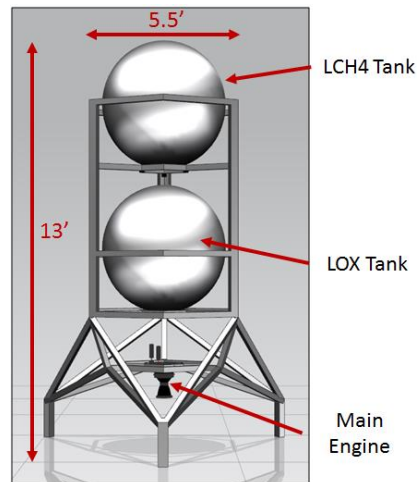


Figure 3.1: Conceptual design of vertical test bed, Janus

Stacking components in vertical form gives greater control authority to the vehicle gimbal, which is the vehicle pitch and yaw control mechanism. As a result, the gimbaled main engine will provide dynamic control for vehicle navigation and stability. The RCS will be providing roll control while in flight. The RCS was limited to roll because a reaction control engine thrust is much smaller than the main engine (5 lbf vs. 2000 lbf), so a gimbal is required for main vehicle control and translation.

Daedalus is a suborbital testbed vehicle which will assess the viability of LOX/LCH4 in vacuum and low gravity conditions, demonstrate main engine restartability and throttability, and assess RCE and main engine propulsion system integration. Daedalus will help further advance and understand LOX/LCH4 technology, since the specified propellant combination has had limited use in vacuum conditions⁵. The propulsion system for Daedalus includes a 500 lbf LOX/LCH4 main engine and a minimum of 12 7 lbf LOX/LCH4 RCEs for attitude control; also, the system uses a regulated helium pressure source. In order to achieve a low orbit altitude, Daedalus will be launched from Earth as the payload off a Terrier Mk 12 sounding rocket. Based on the launch vehicle requirements Daedalus can have a max diameter of 15.75 in., a max overall length of 200 in., and a maximum weight of 500 lbm⁶. Due to these requirements, the physical

⁵ (Klen)

⁶ (NASA Sounding Rockets User Handbook, 2015)

attributes of Daedalus will resemble more of a “missile” shape and components such as propellant tanks will be designed to be cylindrical and not spherical. Figure 3.2 details the design envelope and key components of Daedalus

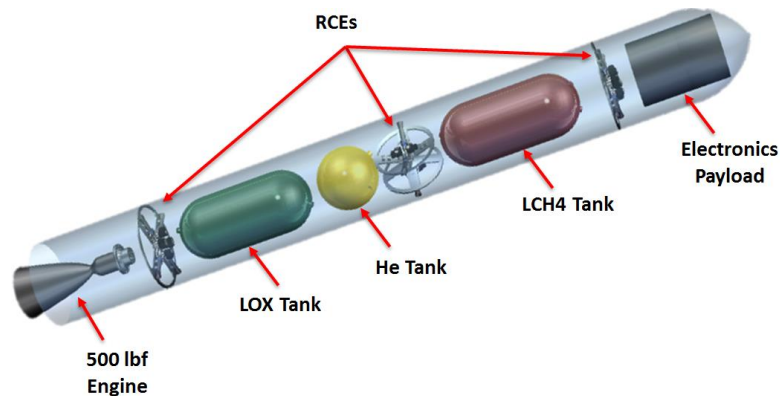


Figure 3.2: Conceptual design of suborbital test bed, Daedalus

3.2 Vehicle Flight Profiles

The flight profile of Janus was chosen to be a takeoff-hover-landing maneuver as shown in figure 3.3 below

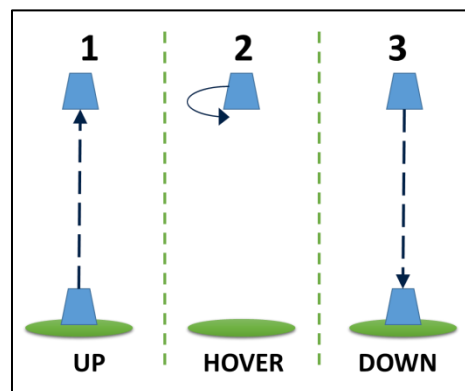


Figure 3.3: Janus flight profile

The vehicle will perform ascent-descent maneuvers before performing any lateral maneuvers. The initial rise maneuver is expected to last around 10 seconds and take the lander to around 20 feet high. Next, the vehicle will hover in place and roll 180° for another 10 seconds.

Finally, Janus will descend for a soft landing in another 10 second maneuver, ending a projected 30 second flight. The flight profile specified will allow operation of the main engine over a range of thrust levels, employ the RCS, and show dynamic control and stability of the lander.

Daedalus is planned to be launched from a Terrier Mk 12 sounding rocket over the Atlantic Ocean from Wallops Flight Test Facility. The following steps outline the beginning of the flight profile for Daedalus: Daedalus will be taken to an altitude of 90 miles above sea level, it will release from the sounding rocket, the data acquisition system will activate, and the vehicle will begin its flight maneuvers. Before performing any flight maneuvers Daedalus will fire its' RCEs to orientate the vehicle perpendicular to Earth's surface. Once the vehicle is orientated the main engine and RCS will go through a series of five engine starts and reorientations. The main engine will be throttled and restarted to demonstrate engine performance and to show reliability within vacuum conditions. Also, the main engine and RCS system integration will be studied to ensure all engines could function properly from a single pair of propellant tanks. Once the flight maneuver has been completed Daedalus will then reenter the atmosphere and deploy parachutes allowing the vehicle to splash down into the ocean to be recovered for analysis. Figure 3.4 depicts the flight profile of Daedalus from start to finish

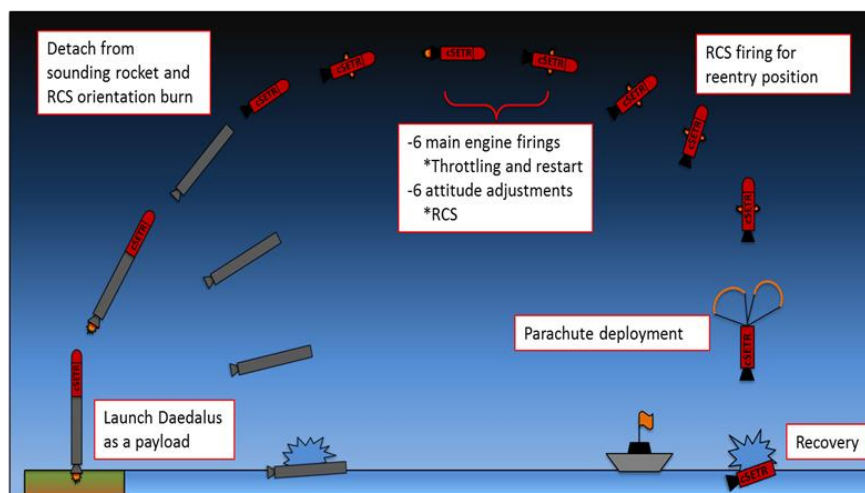


Figure 3.4: Daedalus flight profile

3.3 Vehicle Development

Both Janus and Daedalus will be broken up into three major prototype developments which will allow for a simplified design process. Having a developmental process that includes prototypes for the vehicles allows for gradual improvements to the vehicle design and short-term goals to be met. The prototypes for Janus and Daedalus will be denoted as J-1, D-1, J-2, D-2, etc. J-1 and D-1 will both be static test beds that will allow for the testing of the engines and the propellant delivery systems. After completion of J-1 and D-1, J-2 and D-2 will integrate flight hardware that will be used for each vehicle, create vehicle envelopes, and implement control mechanisms into static testing such as the electronics and autonomous control systems necessary to orientate the vehicles. The final and last prototypes, J-3 and D-3, will essentially be the flight vehicles that will perform the flight maneuvers discussed in the previous section. The prototype developments and testing will be conducted off the UTEP campus at a UTEP owned propulsion facility located Far East of El Paso, TX in a desolate area. The J-3 prototype will be flown and tested at this site; however, D-3 will eventually be moved to NASA Wallops for flight and testing. A full prototype description for both Janus and Daedalus can be found in the appendix section of this report.

Chapter 4: RCE Design Requirements

As mentioned in previous chapters, the RCE was designed with a purpose of being integrated into two flight vehicles. The main requirements for each vehicle, both Janus and Daedalus, were for the engine to deliver 5-8 lbf, use LOX/LCH₄ as propellant, and be able to operate at steady state conditions. Although the tanks for both vehicles have pressures of 350-375 psia, a nominal chamber pressure of 100 psia was chosen for design and test purposes. In future iterations of the engine an increase in chamber pressure will be implemented in order to reduce the pressure drop along the propellant feed lines within both vehicles. In order to evaluate predicted performance characteristics of the engine under various conditions a software known as “*Rocket Propulsion Analysis*” written by Alexander Ponomarenko was utilized⁷. The software Rocket Propulsion Analysis (RPA) uses NASA Chemical Equilibrium with Applications (CEA) to provide thermodynamic data for numerous fuel and oxidizer propellant reactions. Using this software and rocket propulsion theory the specific impulse, mixture ratio, and the nozzle expansion ratio of the engine could then be determined.

Since Janus and Daedalus operate at different environmental conditions, altitude being a major one, some engine performance characteristics differ from one another. As one will see, this is due primarily to an increase in engine performance at higher altitudes. With regards to the engine design, the primary difference between an engine on Janus to an engine on Daedalus is the nozzle expansion; all other design parameters such as the injector, chamber, and throat remain the same. The following relationships show the theory used for determining specific impulse, the mixture ratio, and the nozzle expansion ratio for the engine⁸

$$\text{Specific Impulse:} \quad I_{sp} = \frac{F}{\dot{w}_p} = \sqrt{\frac{2kRT_c}{g_c(k-1)} \left[1 - \frac{P_e}{P_c} \right]^{\frac{k-1}{k}}} \quad (4.1)$$

⁷ (Ponomarenko, 2015)

⁸ (Brown, 1996)

Propellant Flow Rate: $\dot{w}_p = \dot{w}_o + \dot{w}_f$ (4.2)

Mixture Ratio: $MR = \frac{\dot{w}_o}{\dot{w}_f}$ (4.3)

Area Expansion Ratio: $\frac{A_e}{A_t} = \frac{\sqrt{k \left(\frac{2}{k+1} \right)^{\frac{k+1}{k-1}}}}{\left(\frac{P_e}{P_c} \right)^{\frac{1}{k}} \sqrt{\frac{2k}{k-1} \left[1 - \left(\frac{P_e}{P_c} \right)^{\frac{k-1}{k}} \right]}}$ (4.4)

Based on a chamber pressure of 100 psia and inlet condition properties corresponding to LOX/LCH₄, the nozzle of the engine for Janus was found to have an expansion ratio of 2; this would allow for the nozzle to be underexpanded at the test altitude (El Paso region). The nozzle was decided upon to be underexpanded due to the flow separation and performance loss that occurs with an overexpanded nozzle. The following plot was used to determine the expansion ratio for the nozzle to be used on the RCE within Daedalus

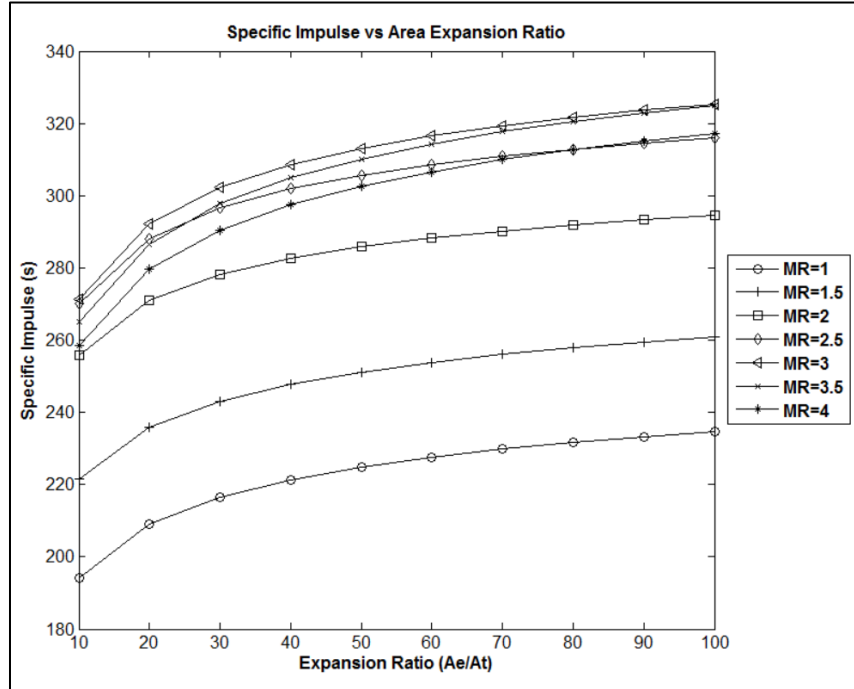


Figure 4.1: Specific impulse vs expansion ratio at varying mixture ratios, $P_c = 100$ psia

From the above plot it can be seen that at all MRs the specific impulse begins to reach an asymptote starting at an expansion ratio within the proximity of $ER = 40$. To reduce weight on the engine, which in turn reduces the total weight of the vehicle, an expansion ratio of 40 was chosen for the nozzle that would be placed on the RCE for Daedalus. From the determined expansion ratios for both vehicles, the following plots could then be generated and analyzed

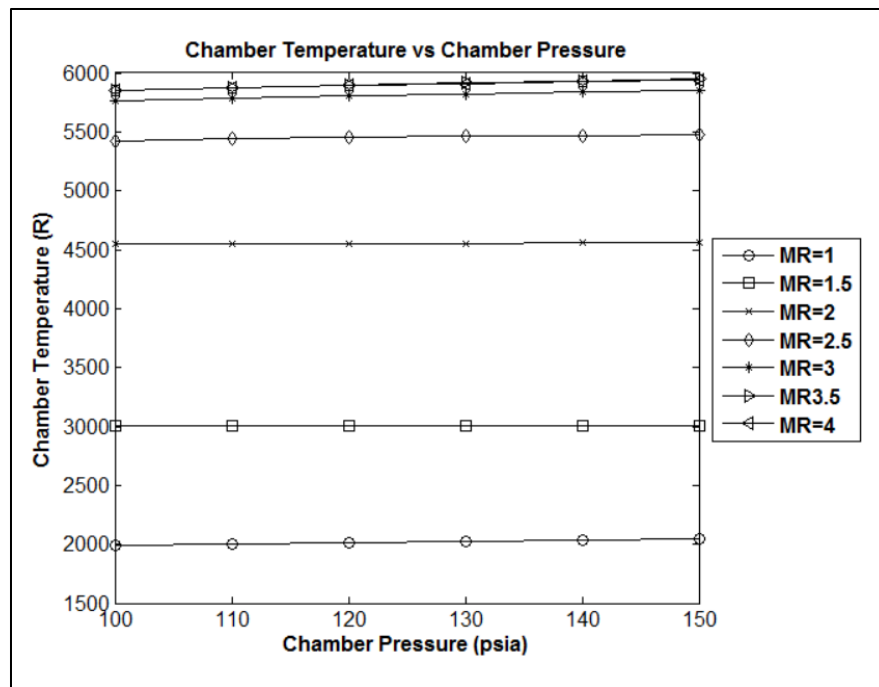


Figure 4.2: Chamber temperature vs chamber pressure at varying mixture ratios

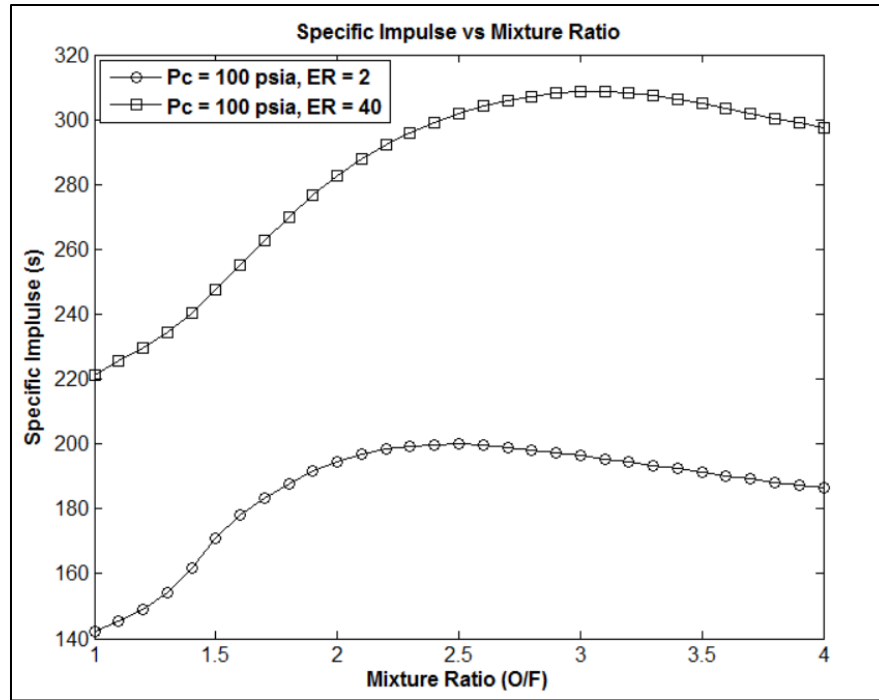


Figure 4.3: Specific impulse vs mixture ratio for Janus & Daedalus engines

Figure 4.3 shows the relationship between engine I_{sp} and MR; it can be seen that in both cases ($ER = 2$ and $ER = 40$) the max I_{sp} is found at an $MR \sim 2.7$. Using an MR of 2.7 would indeed give max I_{sp} potential, but as seen within figure 2.2 at a MR greater than 2.5 the chamber temperature exceeds a temperature of 5500 °R. By simply reducing the MR to 2 the temperature drops a total of 1000 °R to 4500 °R and the I_{sp} is not significantly affected. For these reasons a MR of 2 was chosen for the RCE and I_{sp} values for Janus and Daedalus engines were then calculated. Since the engine would experience high temperature conditions the material that was chosen was Inconel 718 due to its known use within aerospace components and high strengths at elevated temperatures⁹. It was determined that both Janus and Daedalus engines would incorporate fuel film cooling (FFC) with no more than 30% of the total fuel delivered to the engine being dedicated to FFC. With all the requirements set a final MR and I_{sp} could then be determined based on the FFC percentage. The table below highlights the requirements used to design the engine; a detailed RCE requirements list can be located within the appendix section

⁹ (Inconel alloy 718, 2007)

Table 4.1: Top Level RCE Requirements

Requirement	Value
Propellant Combination	LOX/ LCH₄
Operation	Steady State & Pulsing
Material	Inconel 718
Thrust	Janus: 5±0.3 lbf Daedalus: 7±0.4 lbf
Chamber Pressure	100±5 psia
Specific Impulse	Janus: ≥ 182 s Daedalus: ≥ 255 s
Mixture Ratio	2 (Nominal)
Fuel Film Cooling	≤ 30%

Chapter 5: RCE Component Design

This chapter goes into detail on how the components of the RCE were designed; i.e. the nozzle and chamber, injector and manifolds, and the igniter. The engine was designed and fabricated for test purposes at ambient conditions within El Paso, TX. Since the engine was designed not to be flight ready, it will provide preliminary results for the engines that will eventually be placed within the vertical testbed vehicle, Janus. A full engine assembly can be seen and is discussed at the end of this chapter for both testing and flight purposes.

5.1 Nozzle and Chamber Design

The throat area of a nozzle is where choked flow occurs, Mach number is 1, and thus thrust is generated as a result. For these reasons the throat area is generally viewed as the starting point for a rocket engine thrust-chamber design¹⁰. An important parameter in determining the throat area is the thrust coefficient which is characterized as being an improvement in thrust provided by the nozzle. The following relationship relays how the throat area is determined from a theoretical thrust coefficient⁸

$$\text{Thrust Coefficient: } C_f = \frac{F}{P_c A_t} = \sqrt{\frac{2k^2}{k-1} \left(\frac{2}{k+1}\right)^{\frac{k+1}{k-1}} \left[1 - \left(\frac{P_e}{P_c}\right)^{\frac{k-1}{k}}\right]} + \left(\frac{P_e - P_a}{P_c}\right) \frac{A_e}{A_t} \quad (5.1)$$

Using RPA, the thrust coefficient is initially determined from thermodynamic combustion properties of LOX/LCH₄. A thrust coefficient of 1.15 was computed for the specified engine parameters. Using this thrust coefficient, and assuming the chamber pressure and thrust, the throat area was then calculated to be 0.042 in² which corresponded to a throat diameter of 0.23 in. Due to the low area expansion ratio for the Janus engine it was decided that a 15 degree conical nozzle would be implemented for ease of manufacturing. However, since the engine on Daedalus has a higher area expansion ratio a bell nozzle was chosen to shorten the

¹⁰ (Huzel & Huang, Modern Engineering for Design of Liquid-Propellant Rocket Engines, 1992)

⁸ (Brown, 1996)

overall length and increase performance by directing the flow axially at the nozzle exit. Using a contraction ratio of 5 the chamber diameter was found to be 0.5 in. As a result, the contours of the convergent/divergent sections of the nozzles for both vehicle RCEs were developed. The figure below shows a cross sectional view of the two nozzles side by side with the area expansion ratios of each being the lone difference

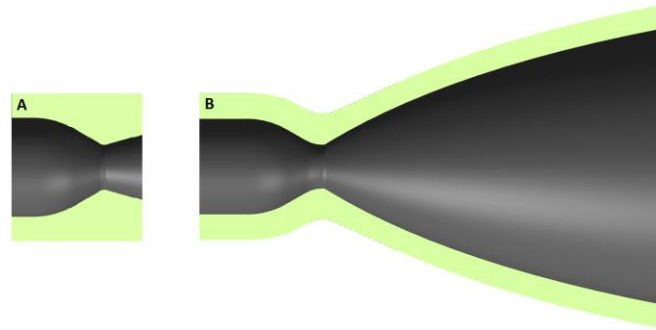


Figure 5.1: Cross sectional view of nozzles for both Janus (nozzle A) and Daedalus (nozzle B) RCEs

In order to have a better understanding of the combustion efficiency produced by the engine, the chamber was designed such that it would be machined to shorter lengths. This would allow the team to analyze the effect of characteristic length, L^* , which is a parameter used to determine the necessary chamber lengths for complete combustion of a propellant combination. The relationship between L^* and the chamber length is shown below

$$\text{Characteristic Length: } L^* = \frac{V_c}{A_t} = \frac{\dot{W}_{tc} v_{ts}}{A_t} \quad (5.2)$$

From equation 5.2 it can be seen that L^* is directly proportional to the chamber volume. If the chamber diameter and throat area of an engine are fixed then L^* is dependent primarily on the chamber length. It should be noted that the chamber length of a rocket engine is generally denoted as the length from the injector to the throat. For the RCE that was designed characteristic lengths of 12 in., 10 in., and 8 in. were chosen to be studied in hot fire testing. Since the engine would eventually be cut the initial length of the chamber was machined to an L^*

of 12 in.; once the first round of tests were completed with this chamber length then the chamber could be cut and re-welded. Subsequently, it would be near impossible to accurately measure from the injector to the throat once the engine components were welded together; therefore, markers on the chamber were machined in order to indicate where to cut. Figure 5.2 specifies the regions to be cut, as shown by the markers, and the re-weld location

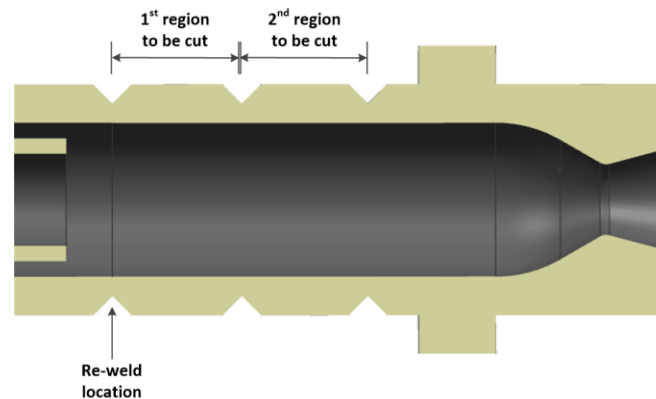


Figure 5.2: Cross sectional view of the chamber showing regions which would be cut to reduce chamber length and further study L^* effects

5.2 Injector Design

The injector design of the RCE is based on previous engine studies conducted by both cSETR and NASA personnel. Thus, the injector configuration was not altered but rather optimized for the performance requirements set by the engine. The geometry of the injector is as follows: a manifold with impinging elements for LOX, a manifold with transverse shearing elements for LCH₄, and lastly a manifold for FFC.

A major reason why the LOX injection elements were designed to impinge amongst each other was the ignition method used by the engine. The ignition method will be spoken in further detail in the next section and a later chapter, but essentially a spark plug is used with an extended electrode tip that arcs along the internal thrust chamber wall. Since this electrode tip is directly down the center of the thrust chamber it creates an obstruction; hence having impinging injection elements for LOX theoretically allows for proper atomization of the fluid. In order to obtain FFC

along the wall of the thrust chamber an internal sleeve, used as a redirection device, was integrated at the location of the FFC injection ports. The figures below relay, in cross sectional views, where the injection orifices are located on the engine and exactly how propellants are injected into the thrust chamber

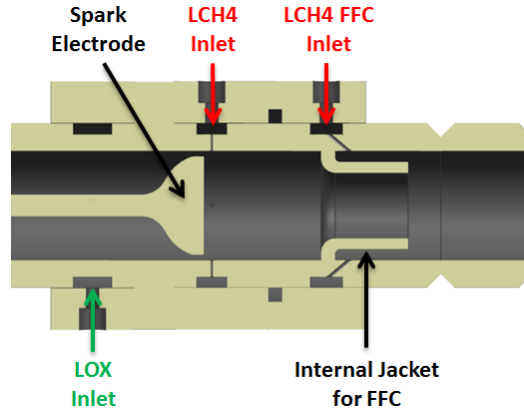


Figure 5.3: Cross sectional view of the RCE detailing injection inlets

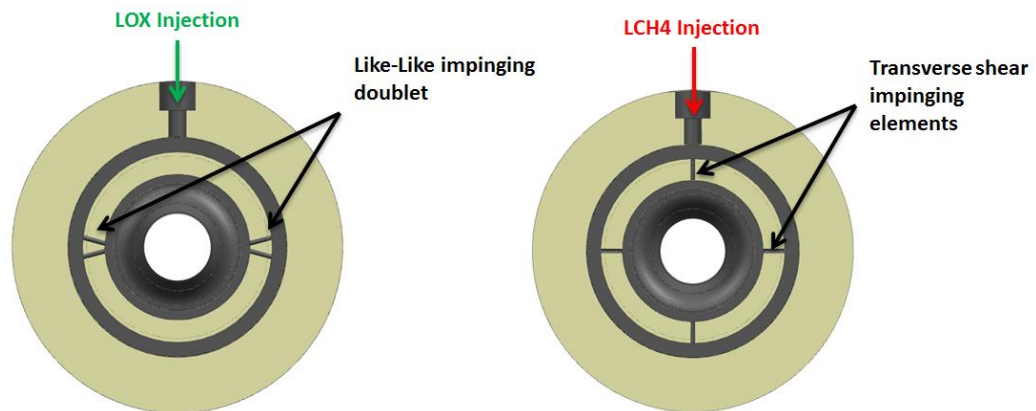


Figure 5.4: Cross sectional view of the RCE injection manifolds for LOX (left) and LCH4 (right)

The propellant manifolds for LOX, LCH4, and FFC are machined separately from the thrust chamber/injector and are later welded on. This allows for the pockets seen in figures 5.3 and 5.4 which are essentially pressurized fluid rings when propellant is allowed to travel through them. Once injected, the LOX travels down the chamber as an annular sheet and is introduced to LCH4 jets slightly downstream of the spark electrode. It is at this region that mixing of the propellant combination occurs and an ignitable mixture ratio is achieved. Simultaneously, as

LOX and LCH4 are being injected so is the fuel for film cooling. As seen in figure 5.3 the FFC injection ports are injected at an angle from the pressurized FFC pocket; this allows for a horizontal velocity of the fuel upon entry of the thrust chamber. Once the fuel for film cooling has reached the internal jacket it is then projected upwards towards the internal thrust chamber wall.

The injection orifices for both LOX and LCH4 were sized based on the mass flow rates derived from the engine requirements, the required pressure drops across the injector, and an assumed discharge coefficient across the injector. The equation below describes the relationship between injection area and the parameters mentioned with regards to injection orifice sizing¹¹

$$\text{Injection Pressure Drop:} \quad \Delta P_i = \frac{1}{2g_c\rho} \left(\frac{\dot{w}}{C_d A} \right)^2 \quad (5.3)$$

One of the assumptions that needed to be made within equation 5.3 was the discharge coefficient across the injector. Since the injector contained sharp edge orifices, C_d was assumed to be 0.65 based on literature¹². Once this parameter was assumed, and using engine requirements, the injection area for both LOX and LCH4 could be found by solving for A within equation 5.3. The orifice diameters resulting from the injection areas calculated for LOX and LCH4 were 0.018 in. and 0.016 in., respectively; both LOX and LCH4 had 4 orifices each. The FFC injection orifices were sized to 0.020 in. each and were designed to be equally spaced radially along the diameter of the engine; the mass flow rate across the FFC injection orifices would be regulated far upstream within the fuel delivery lines by a needle valve.

5.3 Ignition Method

The ignition source on the RCE is a commercially available automotive spark plug. The spark plug is integrated into the thrust chamber upstream of the LOX injector orifices; however, the electrode of the spark plug is extended such that a spark occurs at the region which is a

¹¹ (Huzel & Huang, Design of Liquid Propellant Rocket Engines, 1967)

¹² (Cengel & Cimbala, 2006)

combustible mixture within the thrust chamber. The extended electrode piece was designed to be machined out of tungsten, which has excellent high temperature properties, and welded onto the existing spark plug electrode. Figure 5.5 below illustrates how the designed electrode tip is welded onto the readily available spark plug to create one modified ignition source

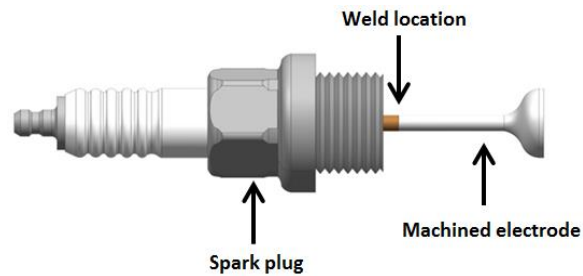


Figure 5.5: Spark plug to machined electrode interface and weld location

The circular feature of the machined electrode allows for a spark to happen along the thruster chamber wall at a point with minimum arc resistance. Figure 5.6 displays where a spark could potentially occur within the thrust chamber

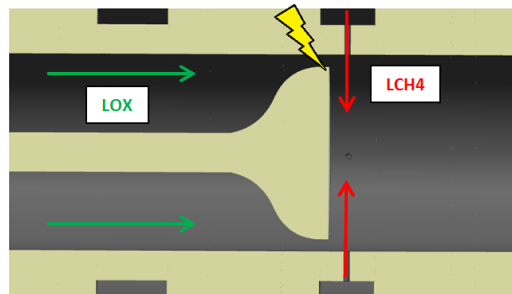


Figure 5.6: Potential arc location (yellow indicator) of the spark electrode to the thrust chamber

To achieve a spark at the electrode the ignition system was designed to use a signal generator, a 12 V car battery, and a transformer coil to send a high voltage (~ 30 kV) to the electrode. By using a relay, a 100 Hz square wave can be transferred on command to the coil which is also connected to the 12 V battery and a spark can then be generated.

5.4 RCE Assembly for Testing and Flight

To conclude the design process of the engine, the RCE was designed to be fabricated and assembled primarily for test purposes which included studying nominal thrust at various inlet conditions, researching the minimum film cooling percentages allowed for safe operations, and understanding the effects of c^* by shortening chamber lengths. Figures 5.7 and 5.8 show both the external and cross sectional views, respectively, of the RCE assembly and highlight the methods for which propellants are delivered to the engine

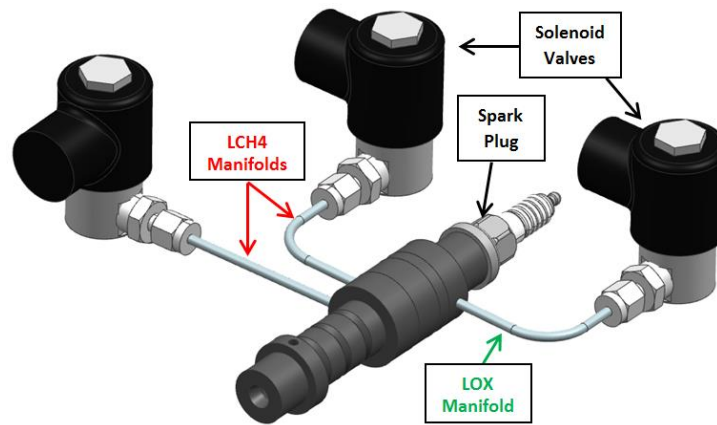


Figure 5.7: RCE assembly to be fabricated for test purposes

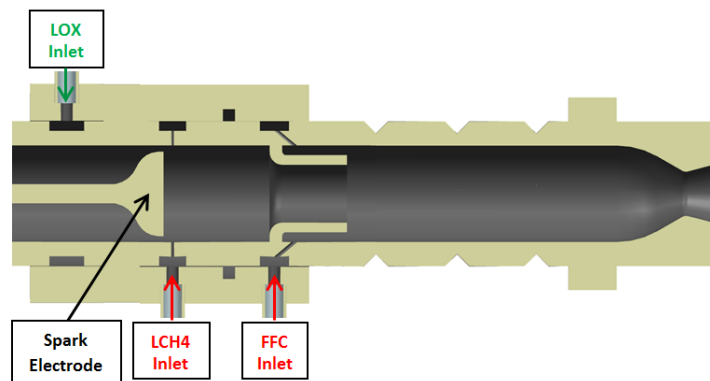


Figure 5.8: Cross sectional view of the RCE assembly for test purposes

The above figures express the overall design of the RCE for test purposes; however, they do not show how the RCE will be configured for flight purposes. Once testing of the RCE is

complete a second design of the engine will look into a more flight like engine that will be integrated into the test programs for both Janus and Daedalus; and, eventually onto the final flight vehicles. A significant change between the flight engine and the testing engine are the propellant manifolds. The flight engine will have one propellant manifold for LOX and one propellant manifold for LCH₄; also, the length of the manifolds will be significantly reduced much like the previous engines researched by NASA JSC and former cSETR researchers. In reducing the propellant manifolds the dribble volume of propellant, volume of propellant within the lines between the main valve and the injector, is significantly reduced thus the minimum impulse bit is reduced as well. Having one propellant manifold for fuel will allow for one valve, instead of two, consequently reducing the overall weight of the engine and the vehicle. The engine will still be film cooled by initially setting a film cooling percentage in the requirements and designing the injector orifices based on this amount. In testing the effects of chamber length, or L^* , with the test purpose engine the RCE for flight will have an optimal chamber length that will allow for the following: sufficient combustion, shorter length hence the ability to properly film cool through the chamber and nozzle, and a reduction in mass. Figures 5.9 and 5.10 show the external and cross sectional views of the proposed design for the flight RCEs

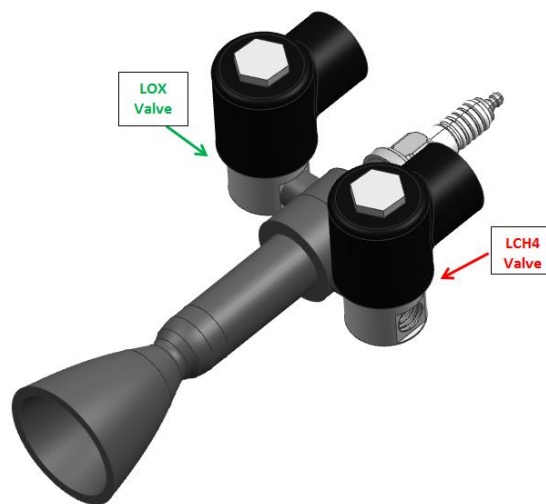


Figure 5.9: Flight design for the RCE to be integrated within the Daedalus vehicle

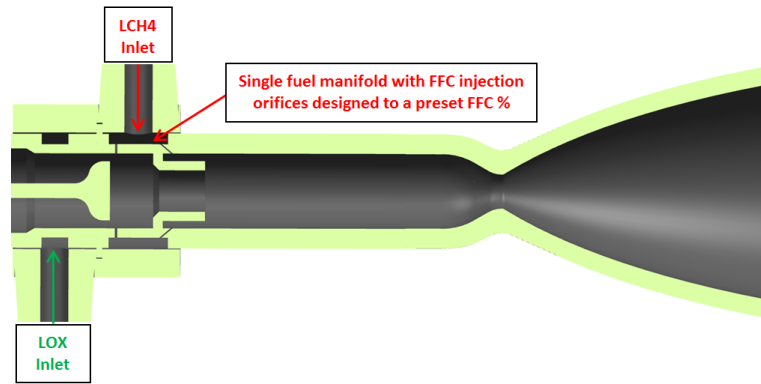


Figure 5.10: Cross sectional view of the flight RCE to be used in the Daedalus vehicle

The above figures display the RCE that will be used for the Daedalus (suborbital) vehicle; essentially all engine components remain the same for the RCEs to be used on Janus except for the nozzle which will have the same area expansion ratio depicted in the engine designed for test purposes (area expansion ratio equal to 2).

Chapter 6: Manufactured Reaction Control Engine

Once the requirements and design phases had been completed the engine to be used for testing could then be manufactured. The contents within this chapter give a brief overview of the machined components, an inspection on key features of the engine, and how the engine was assembled. Within the appendix chapter of this document are drawings of the critical features of the engine such as the chamber (which contains the injector), the nozzle, and the spark plug electrode.

6.1 Chamber and Injection Orifices

The chamber was machined in two parts due to the size of the injection orifices and the complexity of the internal chamber geometry. The first part of the chamber machining consisted of creating the internal and external features of the chamber as shown below in figure 6.1

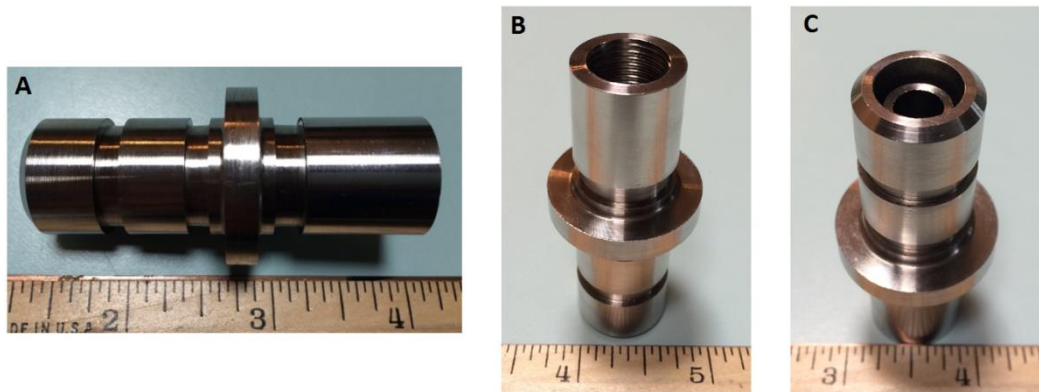


Figure 6.1: Various views of the machined RCE chamber without the injection orifices

Figure 6.1 displays the side (image A), bottom (image B), and top (image C) views of the RCE chamber. In image B the thread can be seen for which the spark plug bolts onto; the size of the thread machined into the chamber is M14x1.25 or spark plug thread. In image C one can see the internal geometry film cooling jacket which is used to deflect fuel towards the wall of the chamber in order to cool it. After the chamber manufacturing had been completed the chamber was sent out to have the injection orifices machined. Due to the orifice sizes, minimum diameter being 0.016 in. for the LCH₄ ports, the machining method that was utilized was electrical

discharge machining (EDM) which uses a heated wire to burn through the material. The injection orifices for both LOX and LCH₄ needed to have tight tolerances due to the pressure drops and flow rates that they were sized for. It was noted that varying these parameters significantly could eventually lead to difficulties with hot fire testing. Figure 6.2 below shows the finished product of the injection orifices that were machined onto the chamber

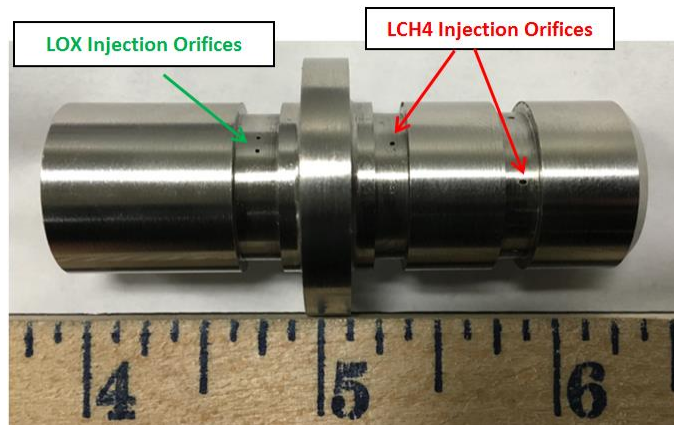


Figure 6.2: RCE chamber with injection orifices machined onto to it

6.2 Nozzle

The critical dimension on the convergent-divergent nozzle is the throat which was designed to have a nominal diameter of 0.23 in. The greater the area of the nozzle the higher the potential risk is for not achieving choked flow at the throat and thus not having the required thrust generated. Figure 6.3 shows both the side view and the top view (looking in through the chamber) of the nozzle



Figure 6.3: RCE nozzle side view (left) and top view (right)

The pressure port which measures the chamber pressure of the engine is located roughly 0.5 in upstream of the throat and is 0.030 in. in diameter. In order to measure pressure from this port 1/8 in. tubing is welded onto the extrusion where the pressure port is located. A pressure transducer is fixed onto the tubing at the other end by use of compression fittings. The location of the pressure port allows for the pressure transducer to measure the chamber pressure at a point which has complete combustion and as a result an expansion of a hot gas. The grooves that can be seen on the nozzle are the markers, or regions, that will be cut and rewelded to the chamber based on the L^* values discussed in the previous chapter. Although the nozzle does not look like conventional nozzles, which are generally solely the convergent-divergent sections, having the elongated barrel section attached allows for easier machining once future testing begins.

6.3 Spark Plug with Extended Electrode

To recall from the previous chapter, the ignition source is a commercially available spark plug which is bolted onto the engine. The spark plug which will be used for this engine is the *Champion Copper Plus Small Engine Spark Plug RJ12C*. Since there is a distance from the LOX injection orifices to the LCH₄ injection orifices the spark plug needed to have a modified electrode in order to spark at a point in the thrust chamber which would allow for combustion. Once the electrode was machined it could then be welded onto the spark plugs electrode by means of laser welding. Figure 6.4 below shows the spark plug with the extended electrode welded on



Figure 6.4: RCE ignition source; modified spark plug with extended electrode tip

6.4 Inspection on Machined Parts

After the engine components had been manufactured they were inspected to ensure that tolerancing had been met, and, were also inspected to give insight into potential differences from theoretical and experimental data. The components were inspected by the use of an electronic caliper that had an accuracy of ± 0.001 in. and plug gauges, specifically Go Gauges, which had accuracy tolerances of $+0.0001$ in. The caliper was used to measure linear and external diametrical dimensions while the Go Gauges were used to measure internal diameters such as the chamber, throat, and injection orifices. The table below gives insight into the machining accuracy accomplished on the features which were of importance to the engine

Table 6.1: Inspection of key features within the RCE

Engine Feature	Designed Value (in)	Actual Nominal Value (in)
Chamber Diameter	0.500	0.499
LOX Injection Orifices	0.018	0.175
LCH4 Injection Orifices	0.016	0.016
FFC Injection Orifices	0.020	0.020
Throat Diameter	0.230	0.239
Chamber Wall Thickness	0.125	0.127

It can be seen from table 6.1 that all tolerances were met for the essential features on the engine; therefore, no manufacturing revisions were necessary. As a result, the engine was allowed to proceed forward with welding and assembly.

6.5 Welded Engine Assembly

In order to assemble the engine, the propellant manifolds needed to be welded onto the chamber first. These essentially were rings that slid onto the chamber and fit into place based on the chamber exterior; each manifold was positioned such that the inlets were perpendicular to the center line of the chamber. After the manifolds had been welded, the nozzle could then be

aligned to the chamber and welded as well. Lastly, tubing with a diameter of 1/8 in. was welded onto the propellant manifold inlets in order to interface between the manifolds and the solenoid valves; the pressure port contained 1/8 in. tubing as well as mentioned in an earlier section. Thermocouples, used to measure high temperatures of the chamber, would later be welded onto the engine which will be shown in the hot fire testing section in a later chapter. Figure 6.5 details the final assembly of the RCE and highlights the locations of the various components

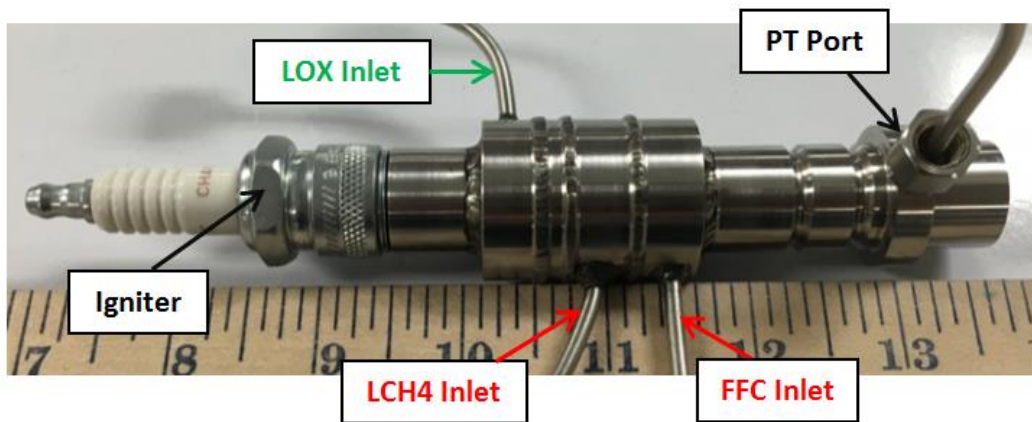


Figure 6.5: Final manufactured and welded RCE assembly

Chapter 7: Cold Flow Testing

In order to have an understanding of the performance and design of the injector, compared to theoretical data, injector water tests were conducted. In performing injector water tests one can obtain injector pressure drop data and mass flow rate data which can then be plotted and correlated to one another. Based on the water test data, predicted data can then be determined for LOX and LCH₄ use by assuming a constant density for the two fluids. These correlations have significant importance because of the test matrices that were and will be developed for hot fire testing. Essentially, knowing the mass flow rates that are obtained from certain injector pressure drops allows for a better understanding of the test system requirements and allows for the development of hot fire test matrices. This chapter will look into the test set-up development and the test results obtained.

7.1 Water Test Set Up

The schematic below is the piping and instrumentation diagram (P&ID) that was used to develop the water test set-up

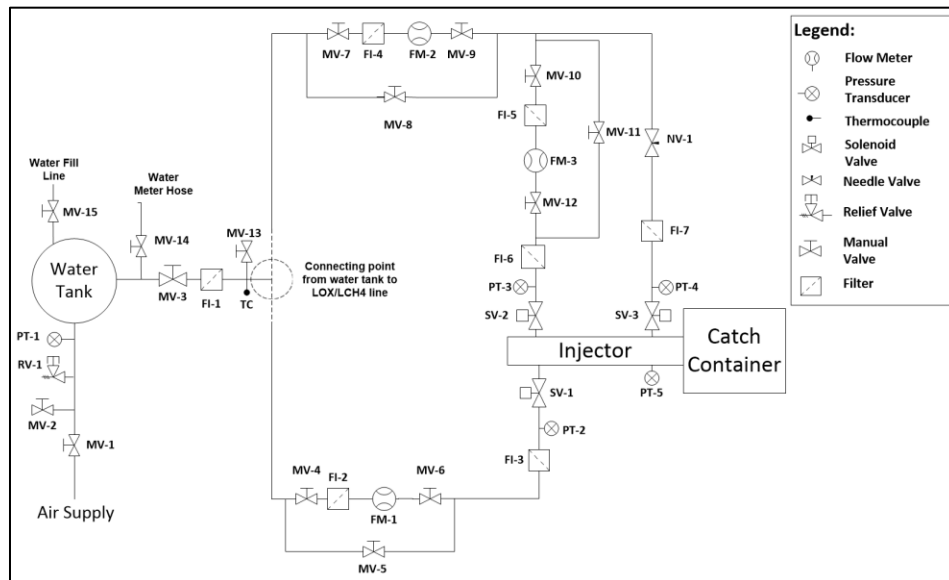


Figure 7.1: Water test piping and instrumentation diagram (P&ID)

The instrumentation used within the set-up consisted of the following: high performance PX309 Omega pressure transducers, Cox loflow turbine flowmeters, and an Omega E type thermocouple to measure the temperature of the water. Gem sensor miniature 12V solenoid valves were used to immediately open and close valves at the beginning and end of a 10 second test. The figures below show the built set up developed within the cSETR lab

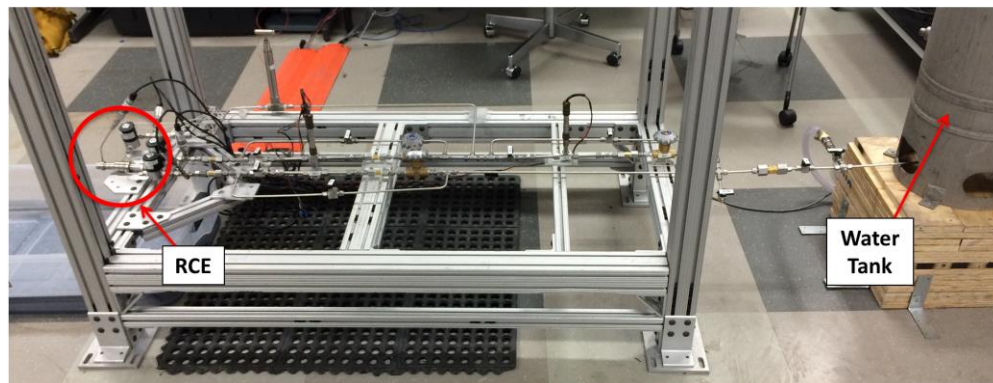


Figure 7.2: Full view of the water test set up from the tank to the RCE

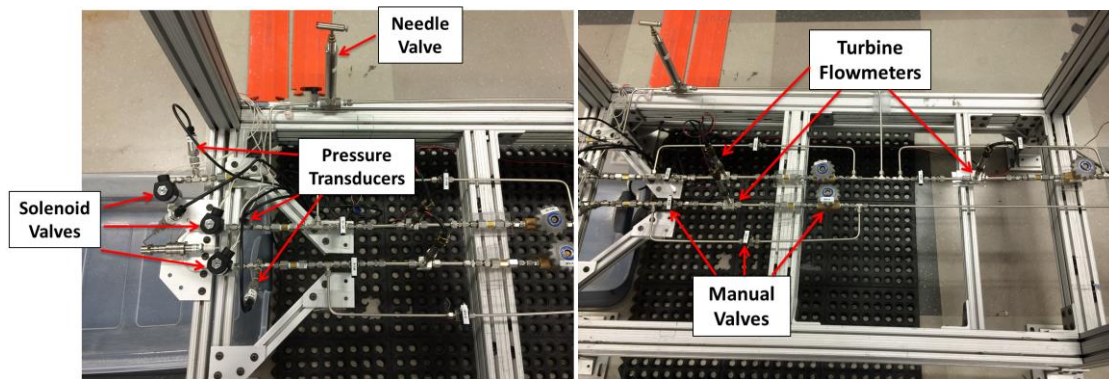


Figure 7.3: Components and instrumentation within the water test set-up

The pressure transducers (PTs) were placed on the water tank and immediately upstream of the engine solenoid valves. The delta P across the injector was recorded as the nominal steady state reading on the PTs upstream of the solenoid valves for both LOX and LCH₄ inlets. This was done because of the fact that the engine was open to ambient conditions and no chamber pressure was enveloped within the thruster during test runs. Turbine flowmeters were used to measure flow rates at significantly small flow ranges between 0.4 lpm to 0.9 lpm; these

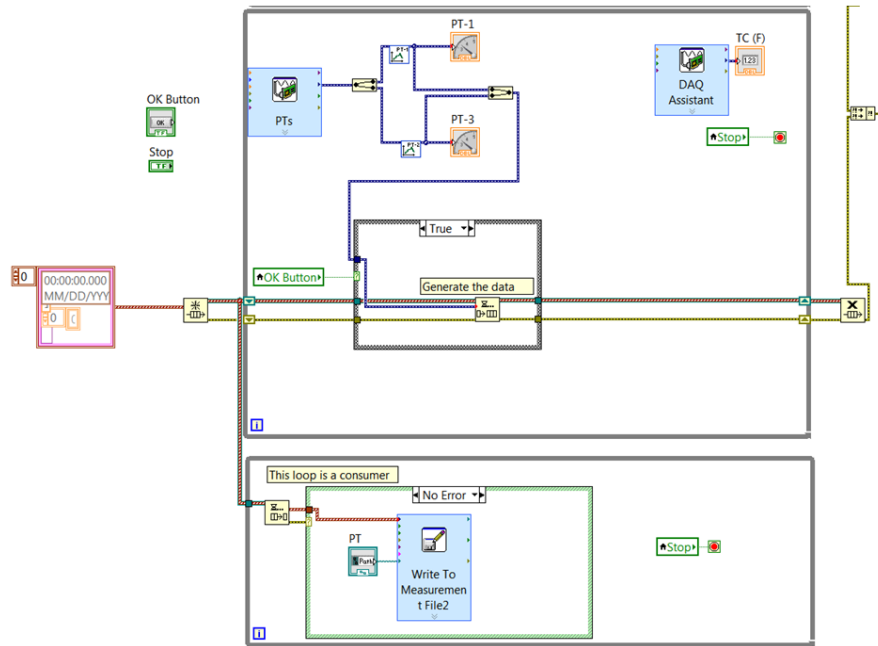


Figure 7.5: Block diagram of the pressure transducer and thermocouple logic

Figure 7.4 details the logic, which incorporated DAQmx tasks, used to read the digital pulse data obtained from the flowmeters; these tasks helped in alleviating issues that would occur whenever the counter on the cDAQ 9171 read 0 Hz (initial state of the flowmeter). In order to account for a significant amount of data being stored a “producer & consumer” logic was implemented for the pressure transducers as shown in figure 7.5. This allowed the system to read the data at the proper frequencies and not overload/crash upon itself.

7.3 Test Results

The test matrices set up for water testing consisted up one independent variable which was the upstream tank pressure. In varying the upstream tank pressure the flowrates at different injector delta pressures could then be found and correlated to one another. As mentioned earlier, the LOX and LCH4 lines were tested individually from one another, but, the test matrices were kept the same for the two. Table 7.1 shows the test matrix developed and the results for both the LOX and LCH4 lines; the raw data pressure and flowrate vs time graphs for both the LOX and LCH4 lines can be found within the appendix section of this report

Table 7.1: Water test results for both the LOX and LCH4 lines

Test Run	Tank Pressure [PSIG]	LOX Injector ΔP [PSIG]	LOX \dot{m} [lbm/s]	LCH4 Injector ΔP [PSIG]	LCH4 \dot{m} [lbm/s]
1	20 \pm 2	19.6	0.017	19.6	0.016
2	30 \pm 2	29.3	0.021	29.3	0.020
3	40 \pm 2	38.5	0.025	38.5	0.023
4	50 \pm 2	48.2	0.027	48.2	0.025
5	60 \pm 2	57.5	0.029	57.5	0.028
6	70 \pm 2	67.5	0.031	67.4	0.030
7	80 \pm 2	77.0	0.033	77.0	0.032
8	80 \pm 2	77.5	0.033	77.5	0.032
9	70 \pm 2	68.4	0.031	68.3	0.030
10	60 \pm 2	58.3	0.029	58.3	0.028
11	50 \pm 2	48.5	0.027	48.4	0.025
12	40 \pm 2	39.2	0.025	39.2	0.023
13	30 \pm 2	29.5	0.022	29.5	0.019
14	20 \pm 2	20.1	0.018	20.1	0.016
15	20 \pm 2	19.9	0.018	19.9	0.016
16	30 \pm 2	29.5	0.022	29.5	0.020
17	40 \pm 2	38.8	0.025	38.8	0.022
18	50 \pm 2	48.2	0.027	48.2	0.025
19	60 \pm 2	57.9	0.029	57.8	0.027
20	70 \pm 2	67.5	0.031	67.5	0.030
21	80 \pm 2	77.1	0.033	77.0	0.031

With regards to uncertainty the LOX line displayed pressure and mass flowrate values that varied nominally between ± 0.5 psia and ± 0.0002 lbm/s respectively. The LCH4 line had a tighter band of uncertainty with the pressure data, which fell within ± 0.3 psia, but the same uncertainty for the mass flowrate as the LOX line. After obtaining the data shown in table 7.1 the discharge coefficient, C_d , values could then be determined for both the LOX and LCH4 lines. The resulting nominal C_d values for the LCH4 and LOX lines were found to be 0.86 and 0.76 respectively. These values were slightly higher than the assumed 0.65 value which indicated that the injector geometry was actually allowing more mass flowrate at a given injector pressure drop. To get a sufficient understanding of the discharge coefficient through the injector values of C_d were plotted against corresponding Reynolds numbers; this correlation gives insight into

whether C_d behaves the same at various flow rates or follows a specific trend in which it might differ at higher or lower flow rates. Figure 7.6 below shows the C_d vs Reynolds number correlations for both the LOX and LCH4 lines

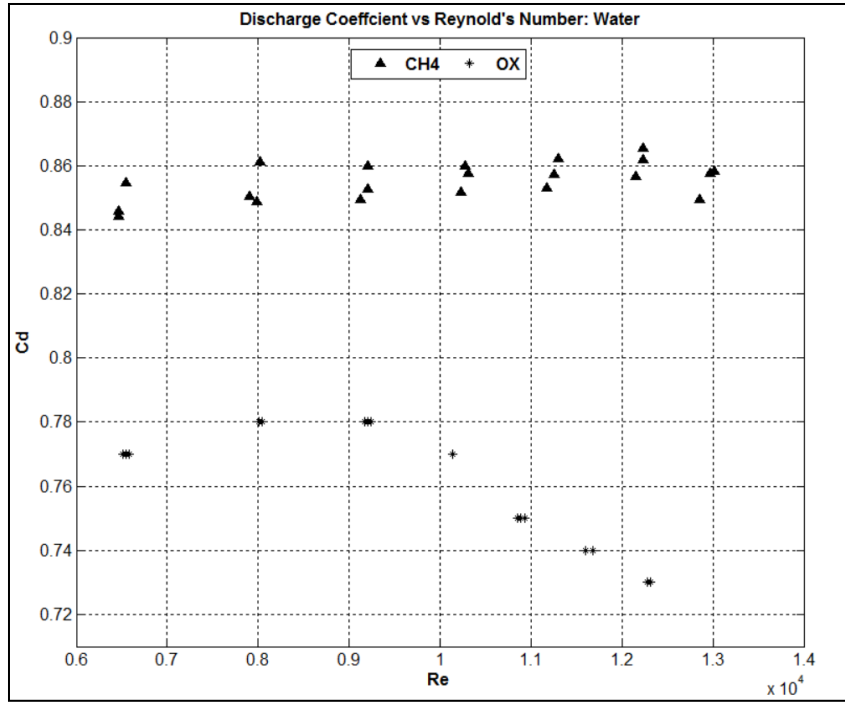


Figure 7.6: Correlation between discharge coefficient and Reynolds number

In figure 7.6 it can be seen that the LCH4 line had a constant C_d at various Reynolds numbers, therefore it was essentially independent of the flow velocity. However, the LOX line displayed a trend in which the C_d was dependent on the flow velocity and decreased as Reynolds number increased. After analyzing and obtaining nominal C_d values, the water test data could then be correlated back to LOX and LCH4 flow rates by changing the density value in the equation shown below which was described in chapter 5

$$\Delta P_i = \frac{1}{2g_c\rho} \left(\frac{\dot{w}}{C_d A} \right)^2 \rightarrow \dot{w} = C_d A \sqrt{2g_c\rho\Delta P_i}$$

In the above equation all values are known, therefore mass flow rates can be determined using LOX and LCH4 properties at specified injector pressure drops. The following two graphs

show the results for the predicted mass flow rates based on an assumed C_d and the predicted mass flow rates of both LOX and LCH4 based on measured C_d data

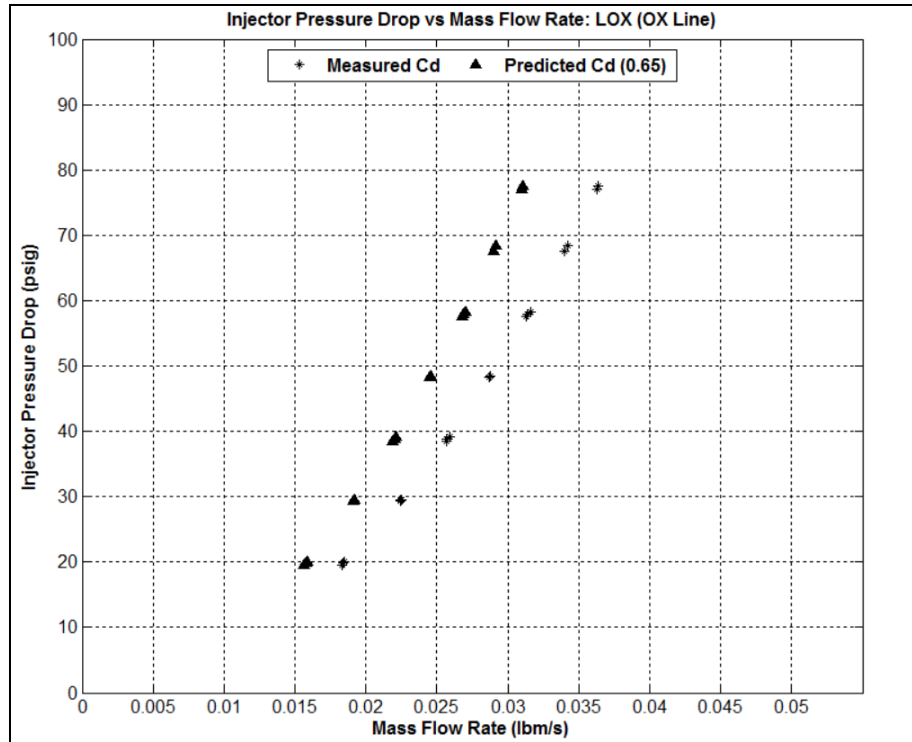


Figure 7.7 Predicted LOX flowrates based on predicted and measured C_d values

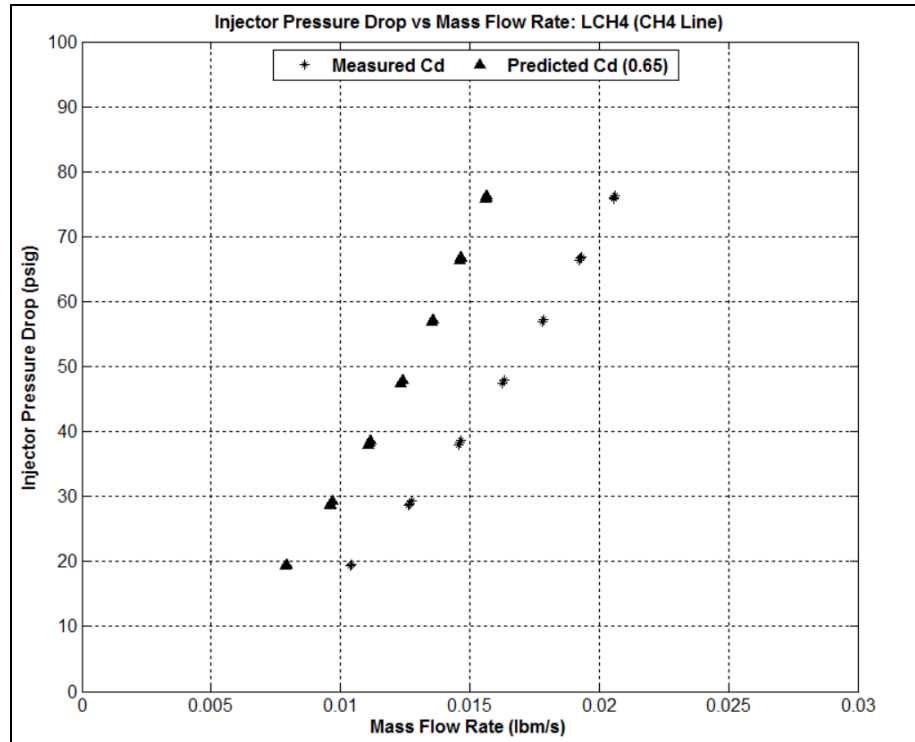


Figure 7.8 Predicted LCH4 flowrates based on predicted and measured C_d values

Figure 7.7 shows that the predicted mass flow rates for the LOX line, based on the measured and predicted C_d values, relate well to each other; the error between the two is less than 15%. There was a slightly larger error for the LCH4 line, around 24%, because of the larger C_d value that was measured through the injector. Thus mass flow rates on the LCH4 line were predicted to be higher than initial expectations in which a significantly lower C_d was being implemented within analyses. As a result of the data, slight changes were made to hot fire test matrices and variables such as upstream tank pressure in order to obtain the required flow rates and mixture ratios.

7.4 FFC Testing and Validation

The last study conducted during cold flow tests was the fuel film cooling test matrix which served as a test validation resource. The matrix was aimed at examining the effect of the needle valve position on the total and combustion LCH4 mass flow rates and also evaluated the

resulting FFC percentages. The table below shows the test results obtained based on varying both the upstream tank pressure and the needle valve position

Table 7.2: Test results for FFC cold flow studies

<i>Fuel Film Cooling Test Matrix</i>						
Test Run	Desired FFC %	Water Tank Pressure [PSIG]	Total \dot{m}_{tot} [lbm/s]	Combustion \dot{m}_{comb} [lbm/s]	Cooling \dot{m}_{cool} ($\dot{m}_{tot} - \dot{m}_{comb}$) [lbm/s]	Actual FFC %
1	5-15%	30±2	0.020	0.018	0.002	10.0
2		60±2	0.028	0.025	0.003	10.7
3		90±2	0.035	0.031	0.004	10.9
4		90±2	0.035	0.031	0.004	10.4
5		60±2	0.028	0.025	0.003	10.6
6		30±2	0.020	0.018	0.002	9.0
7	15-25%	30±2	0.023	0.018	0.005	21.5
8		60±2	0.033	0.026	0.008	22.8
9		90±2	0.041	0.031	0.010	23.3
10		90±2	0.041	0.031	0.010	23.6
11		60±2	0.033	0.026	0.007	22.4
12		30±2	0.023	0.018	0.005	21.2
13	25-35%	30±2	0.026	0.018	0.008	30.4
14		60±2	0.037	0.026	0.012	31.6
15		90±2	0.046	0.031	0.015	32.2
16		90±2	0.046	0.031	0.015	32.5
17		60±2	0.037	0.025	0.012	31.5
18		30±2	0.026	0.018	0.008	30.0
19	35-45%	30±2	0.031	0.018	0.013	42.2
20		60±2	0.044	0.025	0.019	43.6
21		90±2	0.052	0.031	0.021	40.6
22		90±2	0.051	0.031	0.021	40.3
23		60±2	0.044	0.025	0.019	43.5
24		30±2	0.031	0.018	0.013	42.2

The data compiled in table 7.2 was significant in moving forward with hot fire tests for a couple reasons. One observation that was noticed was regardless of the needle valve position the mass flow rate dedicated to the LCH4 combustion inlet was in family with test data that did not incorporate film cooling. This meant that the data found in the previous section could still be utilized efficiently in hot fire tests and the tank set pressures would not have to vary significantly or at all in order to obtain the required LCH4 mass flow rates. Another observation was the FFC percentage did not change due to upstream tank pressure; the FFC percentage was solely dependent on the needle valve position and the cross sectional area for which fluid was allowed to travel through. These two conclusions were key pieces in setting up a hot fire test matrix that would incorporate fuel film cooling and still meet the required mixture ratios for which the engine would be fired at.

Chapter 8: Preliminary Hot Fire Testing

Initial hot fire tests were conducted with the RCE with primary test objectives being aimed towards evaluating engine performance and debugging the experimental set-up for any potential errors. This chapter will discuss the test matrices developed, the test set-up, and the results for both gas/gas and liquid/liquid hot fire tests.

8.1 Test Bunker Facility

The hot fire tests were conducted within the bunker facility at the cSETR propulsion lab. The figure below gives a brief overview of the environment within the bunker and where feed lines, propellant tanks, and the test stand apparatus were located

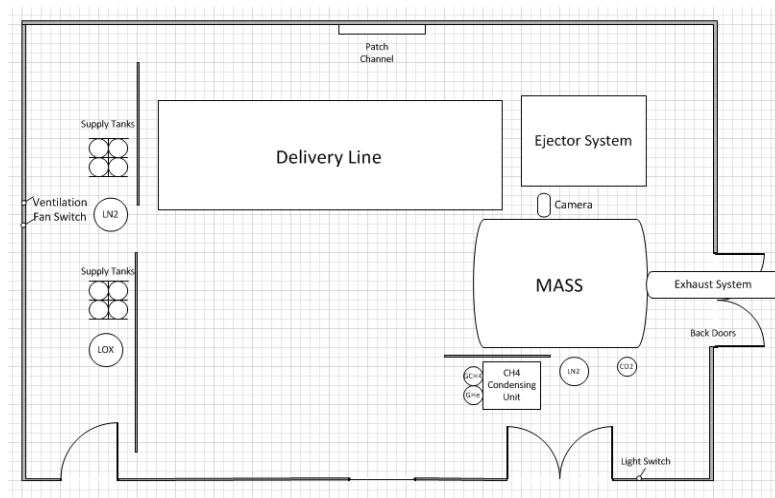


Figure 8.1 cSETR propulsion lab test bunker layout

The multi-purpose altitude simulation system (MASS) is where the thrust stand for testing was placed and where the engine was fired. Detailed piping and instrumentation diagrams for the propellant feed lines can be located within the appendix section of this report. Since both liquid/liquid and gas/gas tests were to be run the set-up was designed to function with various fluid property medias. The instrumentation within the propellant feed lines used for testing included: FMA 1700A/1800A gas flow meters, thermocouples (both K and E type), and PX1005L1-500AV pressure transducers. Flowrates for liquid/liquid testing were measured by

implementing orifices within the propellant feed lines in the place of the gas flowmeters. Since there were only minor changes to the feed system for gas/gas and liquid/liquid testing the liquid/liquid set-up will be the primary topic of discussion. The following figures show the propellant feed lines leading up to the MASS within the bunker



Figure 8.2 LOX feed line to the MASS



Figure 8.3 Methane condensing unit and LCH4 feed lines

Since the lab does not have cryogenic storage for LCH₄, a methane condensing unit has to be implemented into the LCH₄ feed line as can be seen in figure 8.3. Methane in its gaseous state is delivered to the methane condensing unit tank; from here the methane is condensed by significantly cooling the gas. The condensing unit tank contains tubing coils which wrap around the inner and outer walls, liquid nitrogen (LN₂) is delivered through these coils and exhausted into a catch dewar. This heat transfer process allows for condensation of the methane gas at a given pressure and temperature. Thermocouples on the tank indicate the level of liquid within the tank which holds 10 liters.

Both the LOX and LCH₄ delivery lines lead up to the MASS and enter through ports on the bottom of the MASS. The thrust stand is bolted onto the floor of the MASS and the engine is assembled onto the thrust stand. The following figures show the instrumentation and set-up inside the MASS

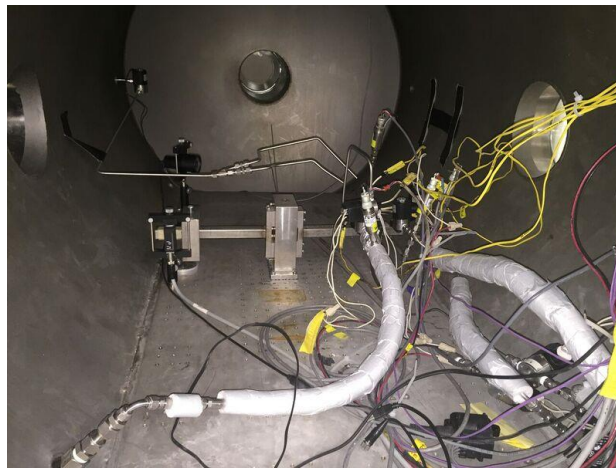


Figure 8.4 Instrumentation and set-up within the MASS

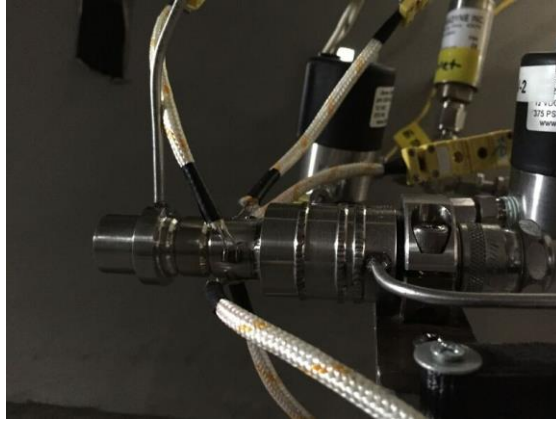


Figure 8.5 Close up of the RCE on the torsional thrust stand

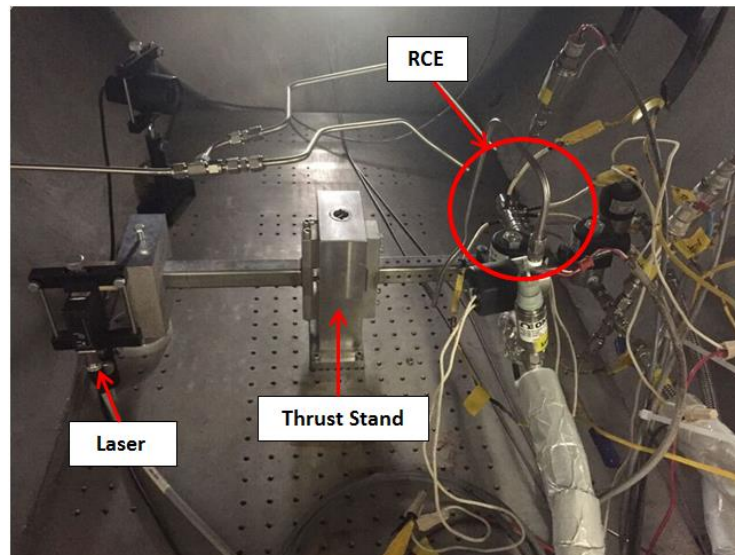


Figure 8.6 Highlighted components within the MASS

In order to measure thrust a torsional thrust stand (TTS) was implemented; this thrust stand was originally designed and used in previous research. Essentially, when the engine fires it displaces the TTS by a small angle and an optoNCDT 1402 laser reads the amount of displacement. This displacement is then correlated back to a calibration curve to obtain a thrust value. Calibrating the TTS with the laser is done by using a pulley system with one end of the cable attached to the TTS at the engine location and the other end attached to a container. When a known weight value is added to the container the TTS displaces further away from the laser location; this displacement is then documented and related back to the weight value (Ex. 5 lbm

displaces the laser by 2 mm). The calibration curve is linear and can be seen below in the following figure

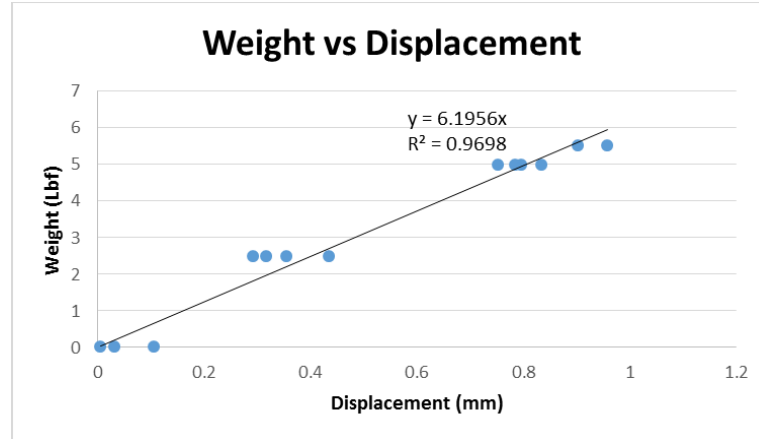


Figure 8.7 TTS calibration data used for thrust measurement

8.2 DAQ and Instrumentation Controller

The LabVIEW controller was essentially the same for gas/gas and liquid/liquid tests thus the back end structure did not change drastically. Data acquisition was similar in nature to that of water testing with slight modifications being made to the sampling rate for instrumentation such as the pressure transducers (1000 samples at 1k Hz). The graphical user interface (GUI) can be seen below for liquid/liquid testing

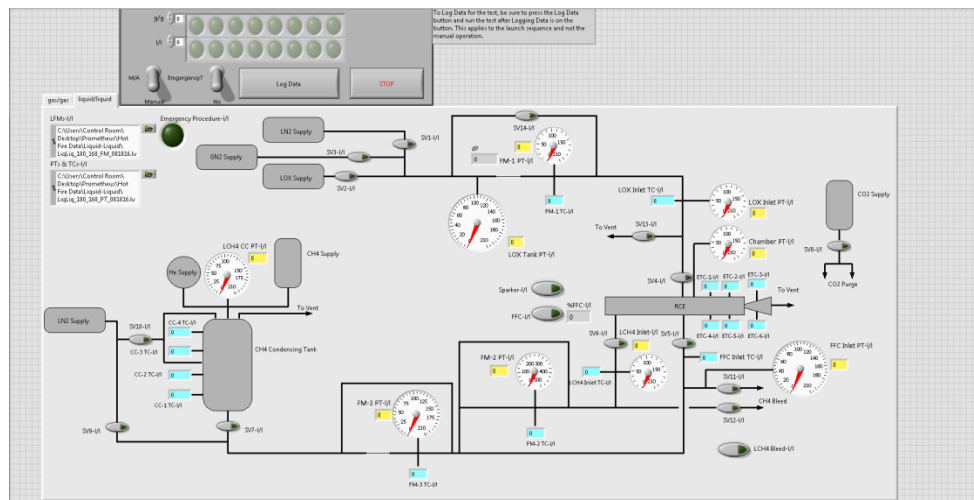
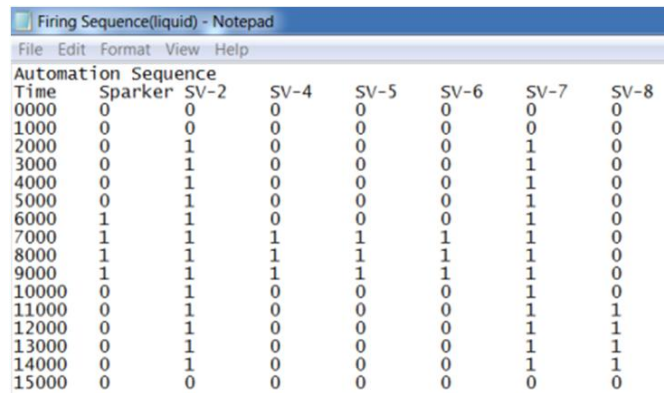


Figure 8.8 Front panel LabVIEW GUI for liquid/liquid testing

The controller has two operating modes: a manual mode that allows the user to open and close valves to condition and feed propellant through the lines, and an automated mode which runs a predefined automated sequence. The automated sequence is loaded in as a text file which is shown below in figure 8.8



Automation Sequence							
Time	Sparker	SV-2	SV-4	SV-5	SV-6	SV-7	SV-8
0000	0	0	0	0	0	0	0
1000	0	0	0	0	0	0	0
2000	0	1	0	0	0	1	0
3000	0	1	0	0	0	1	0
4000	0	1	0	0	0	1	0
5000	0	1	0	0	0	1	0
6000	1	1	0	0	0	1	0
7000	1	1	1	1	1	1	0
8000	1	1	1	1	1	1	0
9000	1	1	1	1	1	1	0
10000	0	1	0	0	0	1	0
11000	0	1	0	0	0	1	1
12000	0	1	0	0	0	1	1
13000	0	1	0	0	0	1	1
14000	0	1	0	0	0	1	1
15000	0	0	0	0	0	0	0

Figure 8.9 Automated sequence loaded into the LabVIEW controller

Within the automated sequence is a list of boolean commands stating whether to leave a solenoid valve open (1) or closed (0). The automated sequence developed was designed for 3 second nominal burn duration firing times followed by a CO2 purge of the engine exterior for 3 seconds. The block diagram portion of the code which reads in the automated sequence is shown in the following figure below

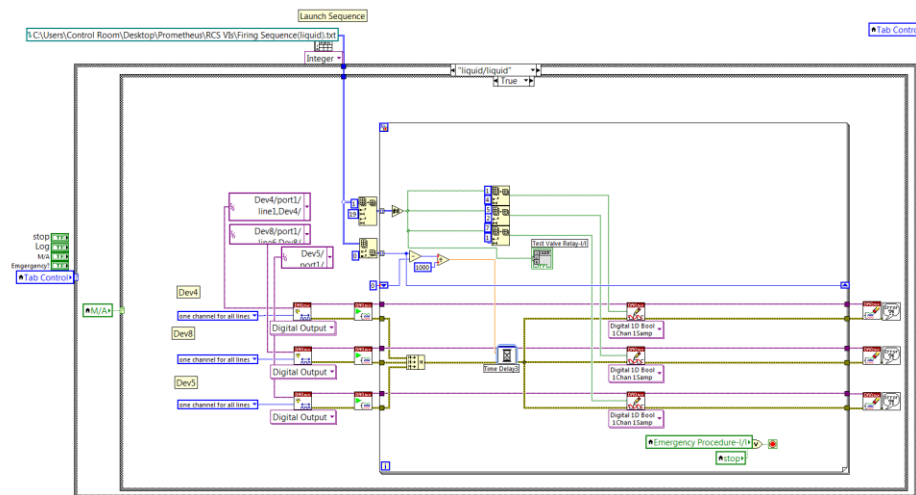


Figure 8.10 Automated sequence block diagram

Redlines were incorporated within the LabVIEW program in the event that a pressure would exceed 230 psia and a temperature would exceed 1200 F. Figure 8.10 shows the nested structures utilized for the solenoid valve control

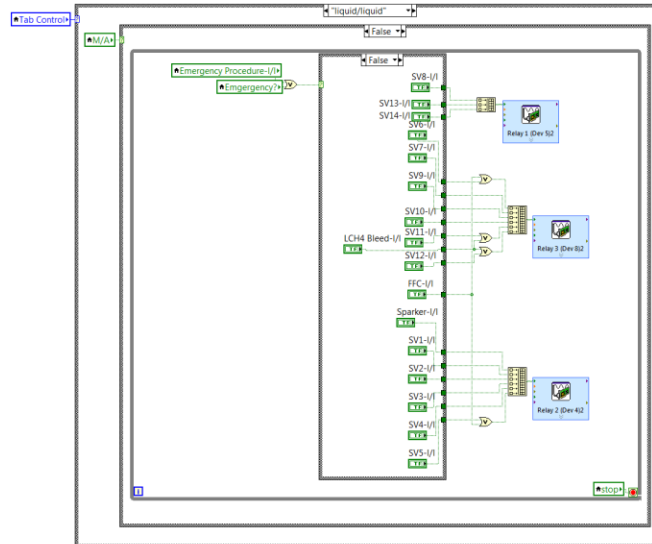


Figure 8.11 Solenoid valve control structure block diagram

Since the redlines were constantly being monitored by the controller, in the event that they were triggered figure 8.10 shows that a pre-defined automated sequence would come into play for which a set of valves would close or open. It should also be noted that once the automated sequence toggle for firing was turned on the while loop was deactivated thus not allowing for manual control from the user.

8.3 Hot Fire Test Results

8.3.1 Gas/Gas Testing

Although the engine was designed for liquid/liquid operation, gas/gas tests were conducted with hopes of understanding how the engine would perform at various inlet conditions and propellant properties. Multiple thermocouples, total of 6, were welded onto the chamber and nozzle of the engine and were used to map out a temperature profile. The placement of the thermocouples along the engine can be seen in the following figure

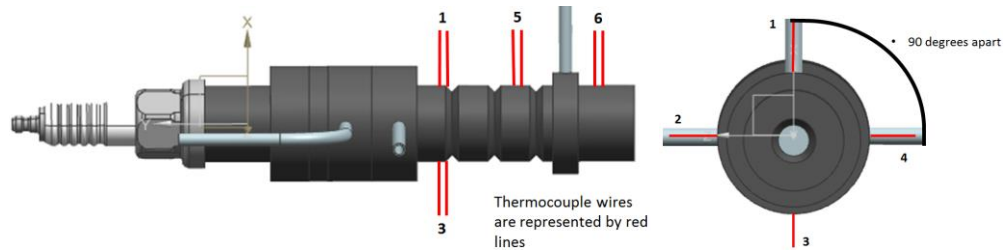


Figure 8.12 Thermocouple locations on the engine chamber and nozzle

To protect the engine from high temperatures all gas/gas tests consisted of film cooling within a range of $30 \pm 5\%$ to total fuel flow. A total of 6 gas/gas tests were completed, but only 3 will be discussed in detail within this section. The following test matrix shows the test points and the resulting data for gas/gas testing

Table 8.1: Hot fire test results for gas/gas testing

Test ID	MR	OX Inlet Conditions		CH4 Inlet Conditions		Mdot		P_c (psia)	F (lbf)
		Press. (psia)	Temp. (F)	Press. (psia)	Temp (F)	OX (lbm/s)	CH4 (lbm/s)		
1	1.83	179.8	72.0	143.8	73.0	0.050	0.028	19.3	0.40
2	1.93	179.7	71.8	134.9	71.5	0.050	0.026	19.1	0.35
3	2.26	179.6	73.4	116.3	73.4	0.050	0.022	18.7	0.29

A couple things immediately stood out from gas/gas testing: the first was that chamber pressure was relatively low compared to prior test history, the second was thrust was also low compared to initial predictions, and finally specific impulse was essentially nonexistent since low thrust was produced and high flowrates were obtained in the process. That being said, a couple positives could be taken away from the gas/gas testing such as thrust values which were in family with previous engines tested at the lab^{13,14}. Also, the engine was well within its' specifications for chamber wall temperature limits, lower than 1200 F, and was able to withstand multiple firings. The following sets of data correspond to each test point in which mixture ratio was the variable parameter

¹³ (Acosta-Zamora, 2012)

¹⁴ (Mena, 2014)

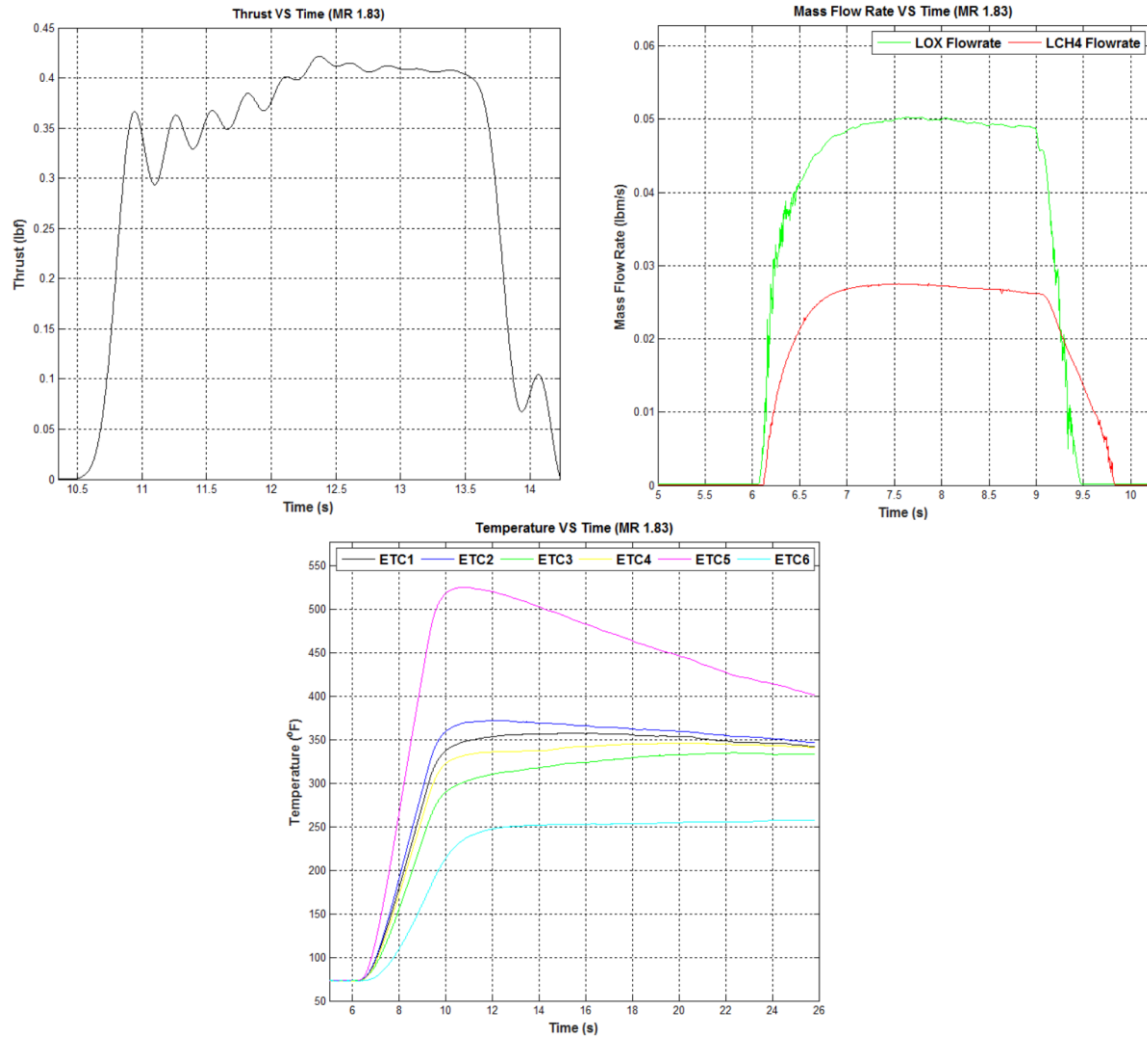


Figure 8.13 Gas/gas hot fire test results for MR=1.83

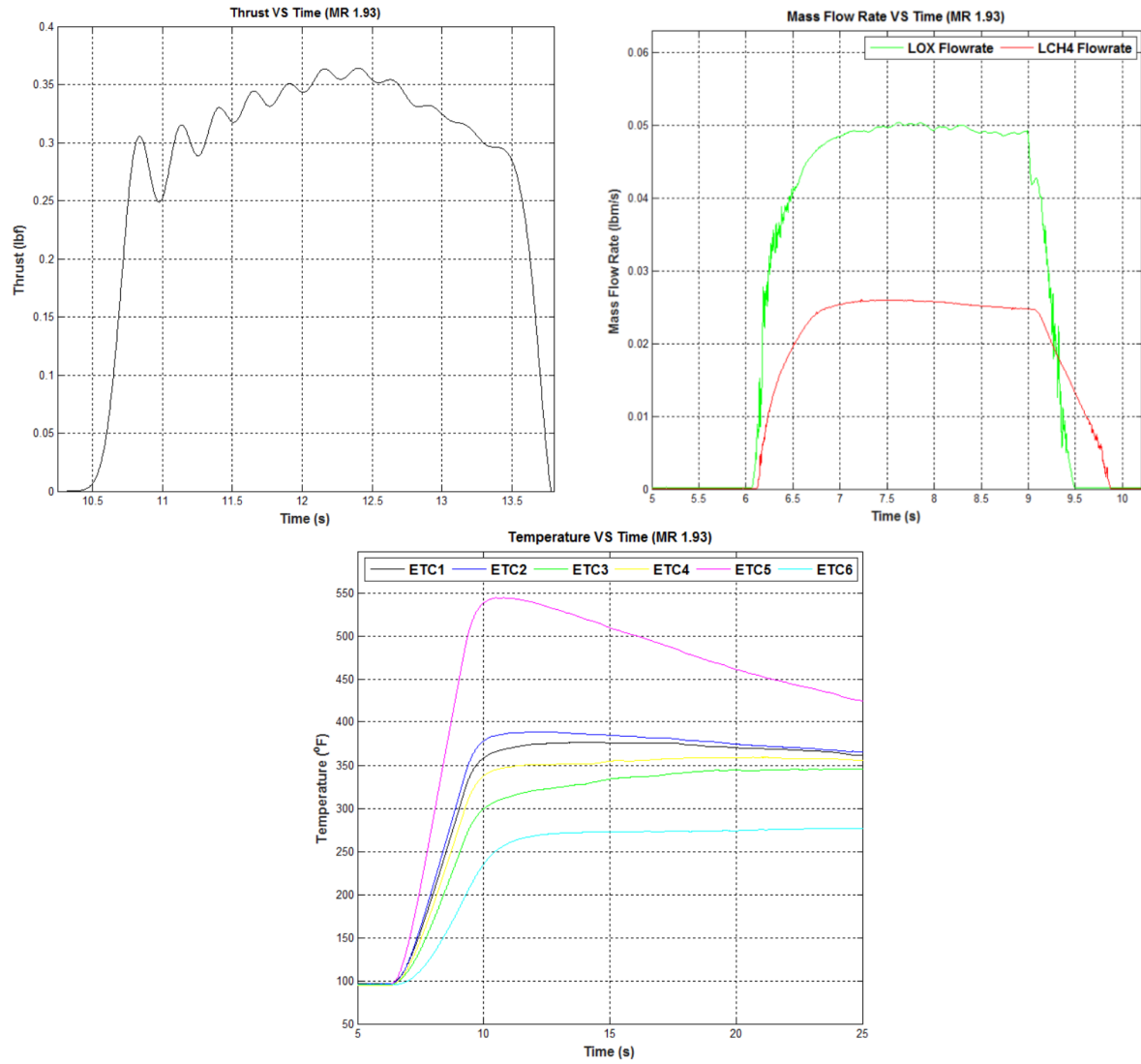


Figure 8.14 Gas/gas hot fire test results for MR=1.93

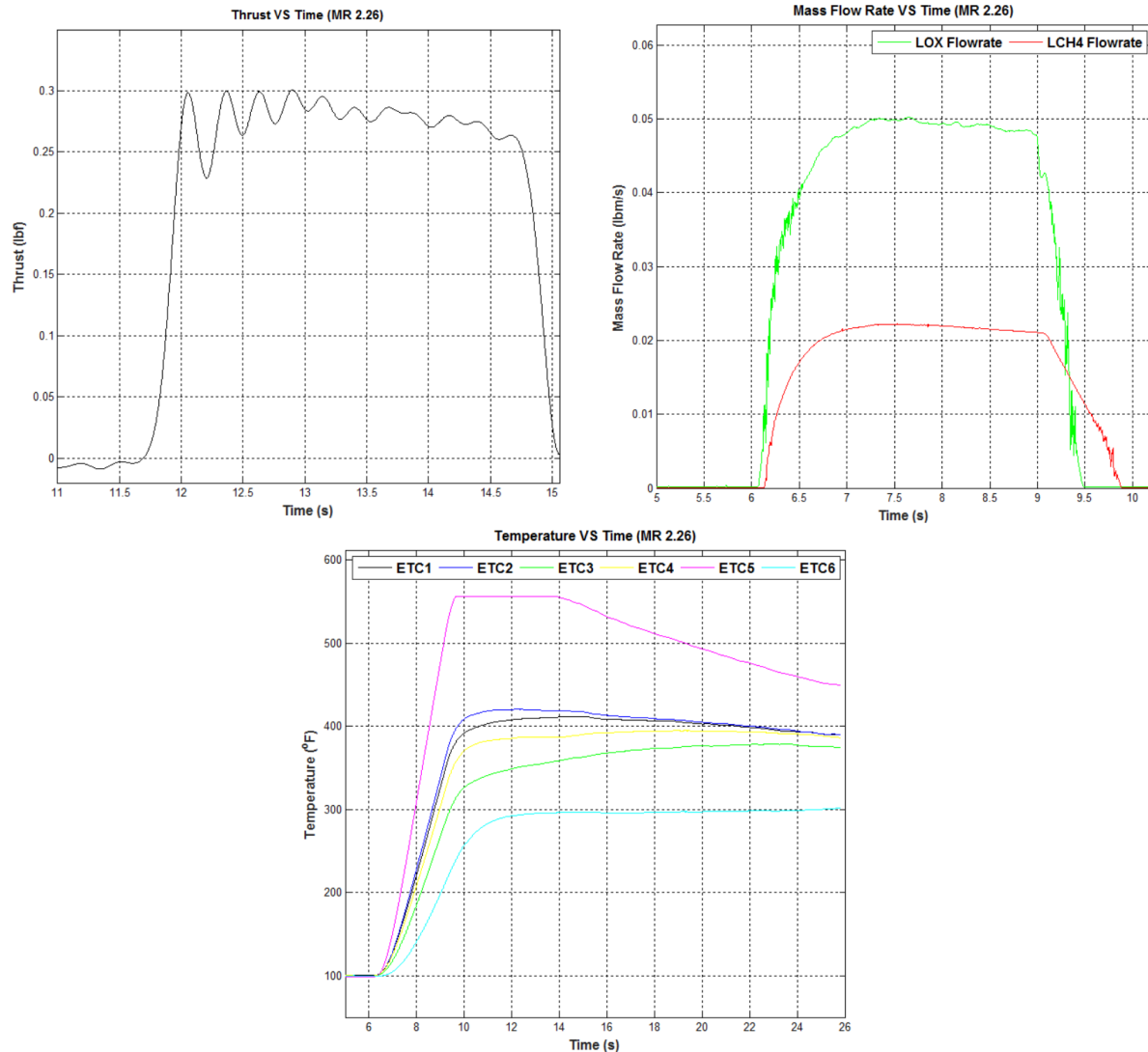


Figure 8.15 Gas/gas hot fire test results for MR=2.26

One reason for believing that the chamber pressures enveloped within the engine were significantly lower than expected was the size of the pressure port orifice. The orifice was designed to be a 0.030 in. diameter hole to restrict a significant amount of hot gas flow to the pressure transducer. However, in machining the orifice to this dimension the flowrate through the orifice might have been substantially small thus not allowing the transducer to properly reach a steady state during the firing duration. Another theory associated with low chamber pressure is the assumption that combustion was happening further downstream of the throat and flow was not being choked. Both theories will lead to further investigation since testing proved

undoubtedly that chamber pressure was consistently lower than expected regardless of mixture ratio or inlet conditions as can be seen in figure 8.16

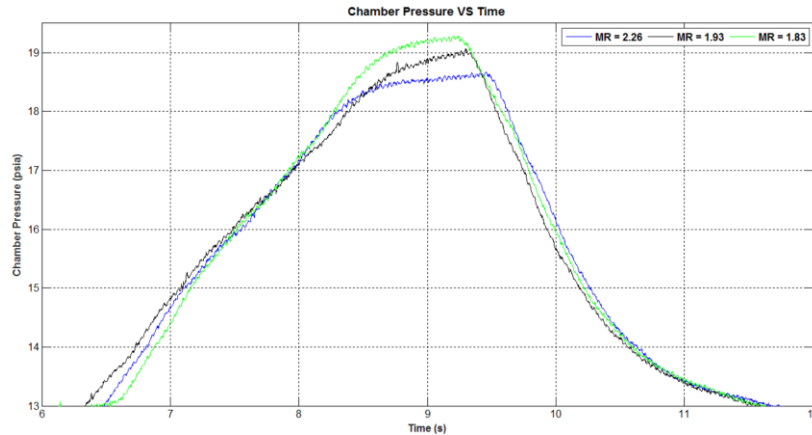


Figure 8.16 Gas/gas hot fire test chamber pressure results

For MRs of 2.26 and 1.93 video inspections showed a somewhat slow startup transient but with regards to the steady state portion nothing was seen to be off nominal when investigating the plume of the exhaust gas. For the low MR test point, 1.83, there were some issues seen with the startup and a well-defined exhaust plume was not evident. The images of each test showing the exhaust plumes can be seen in the images below

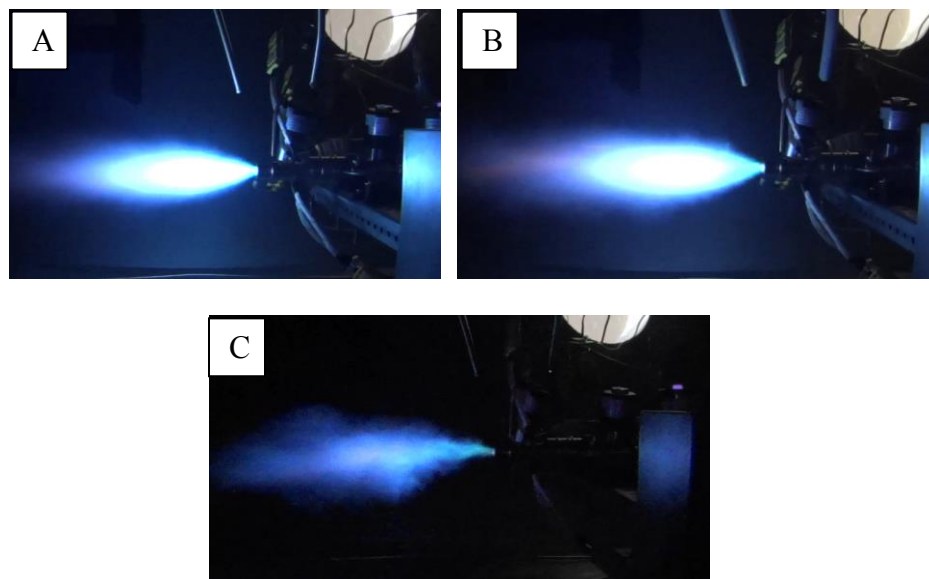


Figure 8.17 Video imaging of the gas/gas tests; A) MR=2.26, B) MR=1.93, C) MR=1.83

8.3.2 Liquid/Liquid Testing

Due to the anomaly with chamber pressure in gas/gas testing the initial test matrix developed for liquid/liquid consisted of multiple tests which would try and evaluate the chamber pressure at low and high mixture ratios. However, since there were initial issues with the FFC valve freezing it was decided that a new test matrix would have to be developed which would run the engine at low mixture ratios without the use of FFC. Three of the tests that were conducted within the new test matrix will be spoken about within this section; the test matrix and results from testing are shown below in the following tables

Table 8.2: Hot fire test results for liquid/liquid testing

Test ID	MR	LOX Inlet Conditions		LCH4 Inlet Conditions		Mdot		P _c (psia)	F (lbf)
		Press. (psia)	Temp. (F)	Press. (psia)	Temp (F)	LOX (lbm/s)	LCH4 (lbm/s)		
1	0.35	120.9	-221.4	70.5	-215.0	0.001	0.004	17.3	0.46
2	0.81	146.4	-232.6	71.8	-152.0	0.005	0.007	18.3	0.40
3	1.15	120.5	-239.0	84.4	-187.0	0.007	0.007	16.5	0.25

Table 8.3: Engine performance results for liquid/liquid testing

Test ID	MR	Isp (s)	C* (ft/s)	Pred. C*(ft/s)	C* eff. (%)
1	0.35	95.8	2550.3	3440.7	74
2	0.81	33.1	2027.8	4173.7	50
3	1.15	18.0	1583.3	4420.4	36

Again, a common trend of low P_c was noticed for the above test results. Thrust was around the same magnitude of gas/gas tests but as with gas/gas remained lower than predicted. The Isp values seemed to contradict theory but this is primarily because at the lower MR less flow rate was seen to produce roughly the same amount of thrust. Also, potential freezing of the flex hoses leading up to the engine could have produced a higher line stiffness over time which in turn would have mean lower thrust seen. The predicted C* values were determined using RPA software and specifying the test conditions till an iteration met the flowrates seen. As with Isp C* efficiency should have been higher as the MR increased, but what was recorded through testing

was a decay in efficiency as MR was increased. In order to better understand the repeatability of the thrust measurement three tests were conducted at the same inlet conditions and the thrust was the key parameter analyzed. Table 8.4 below shows the uncertainty analysis

Table 8.4: Uncertainty analysis on thrust stand measurement

LOX Inlet Pressure = 180 psia, LCH4 Inlet Pressure = 150 psia							
Thrust (lbf)	N	v	Sigma	t	P	R	w
0.62	3	2	0.036	4.303	0.00005	0.089	0.089
0.55							
0.62							

The analysis had shown that an error of ± 0.089 lbf was associated with the thrust measurement system; this value was deemed to be acceptable. The reduced thrust, flowrate, and chamber wall temperature data for each of the MRs is displayed in the following figures

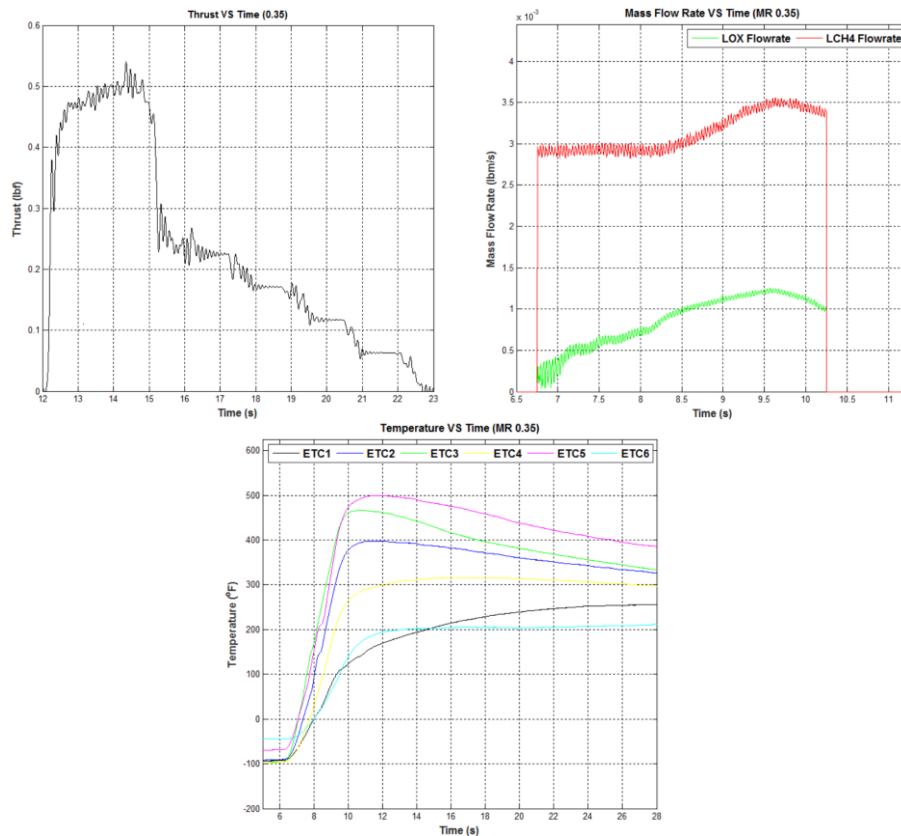


Figure 8.18 Liquid/liquid hot fire test results for MR=0.35

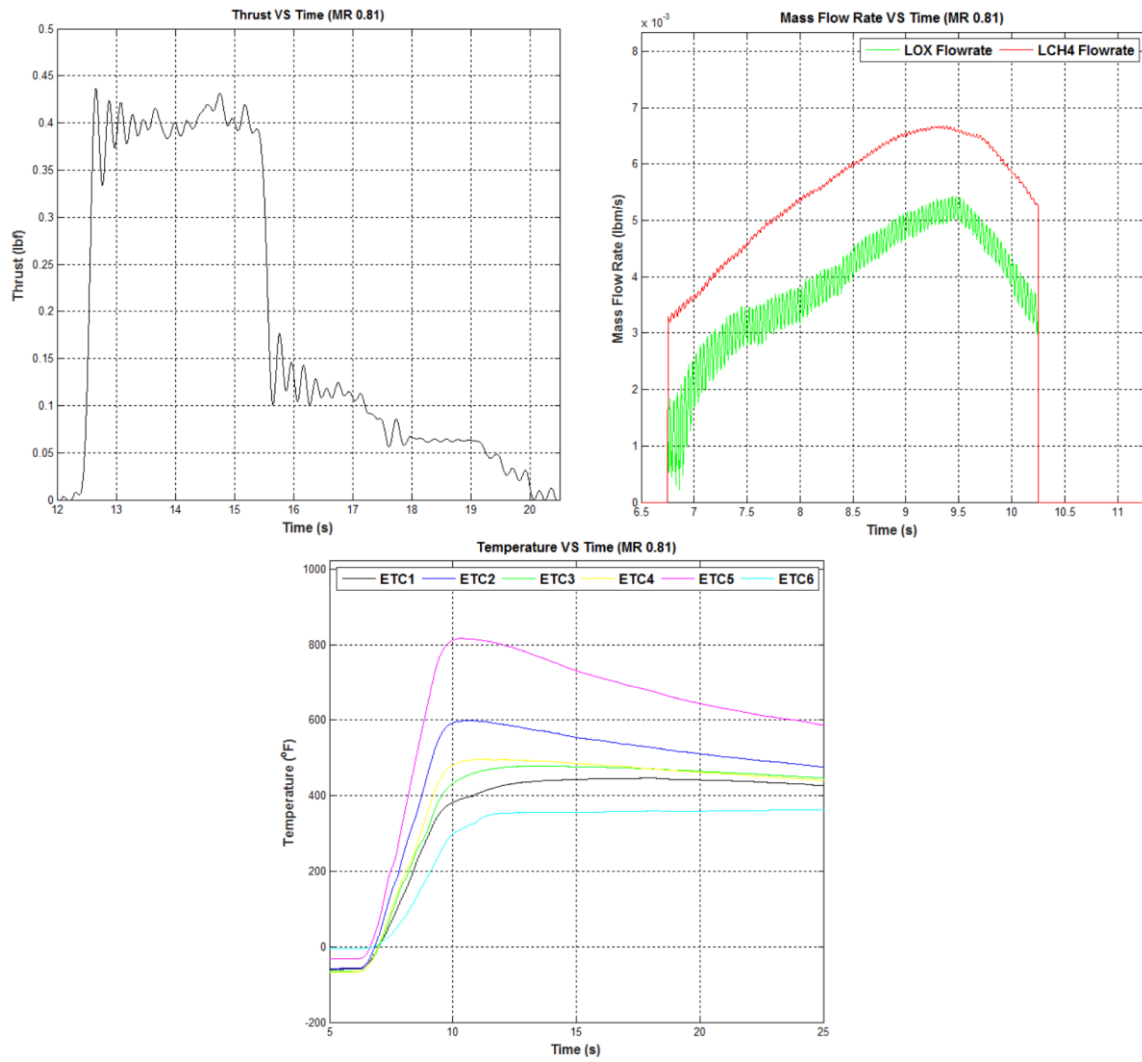


Figure 8.19 Liquid/liquid hot fire test results for MR=0.81

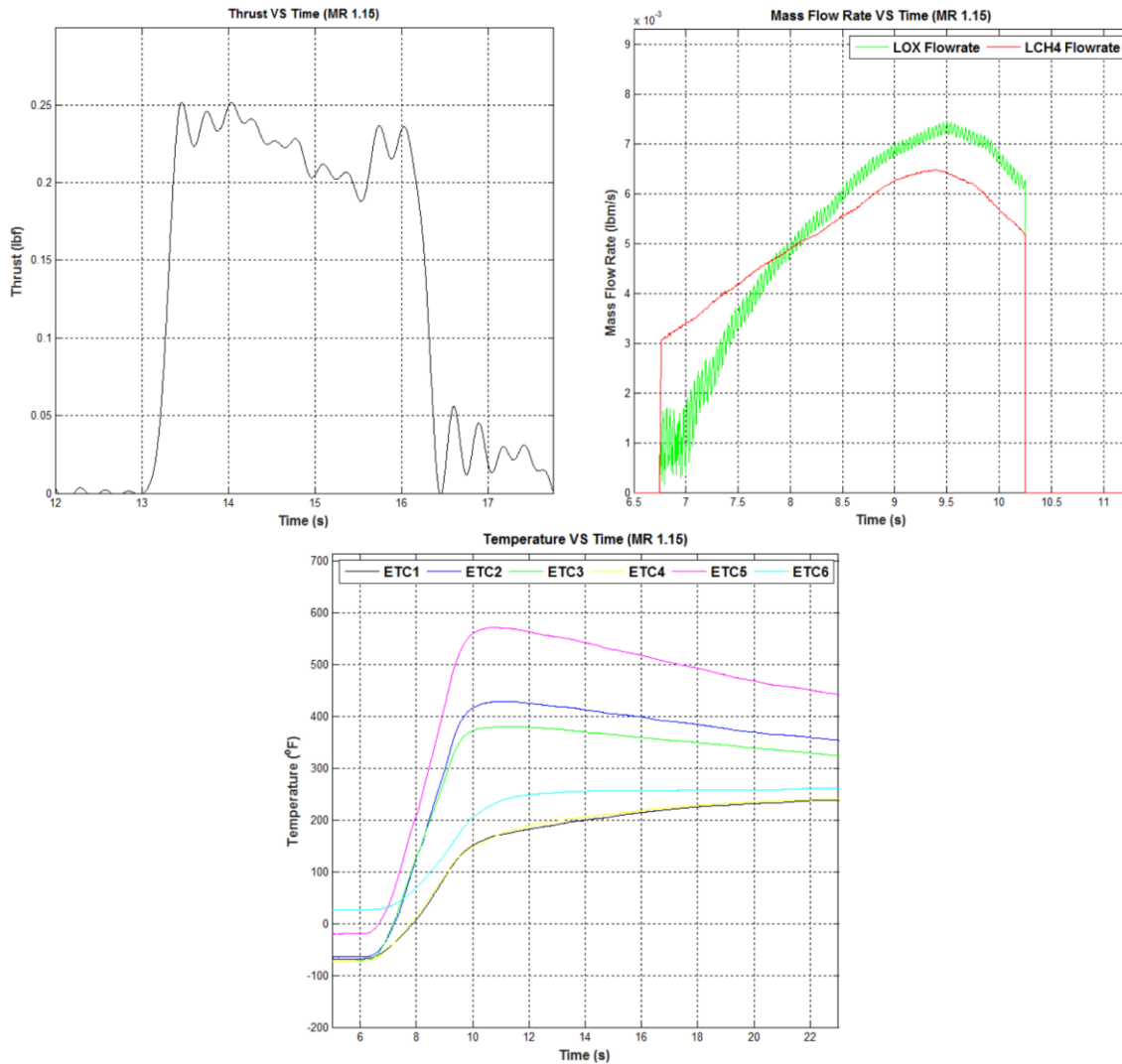


Figure 8.20 Liquid/liquid hot fire test results for MR=1.15

From the previous figures within the thrust plots the total impulse and fire duration appears larger than what it should be for MRs of 0.35 and 0.81, but the firing duration for the 2 test points was only for 3 seconds. After the steady state thrust was reached and the engine valves were closed the thrust would decay, but the thrust stand would take some time to get back to its' nominal starting position which is the long decay to 0 thrust seen in both of the thrust graphs. As with the gas/gas tests the chamber and nozzle temperatures were still well below the redline set; again, the hottest part of the engine as expected was the convergent section of the nozzle (around the throat). The chamber pressures for each test were plotted in the same plot and can be seen in figure 8.21

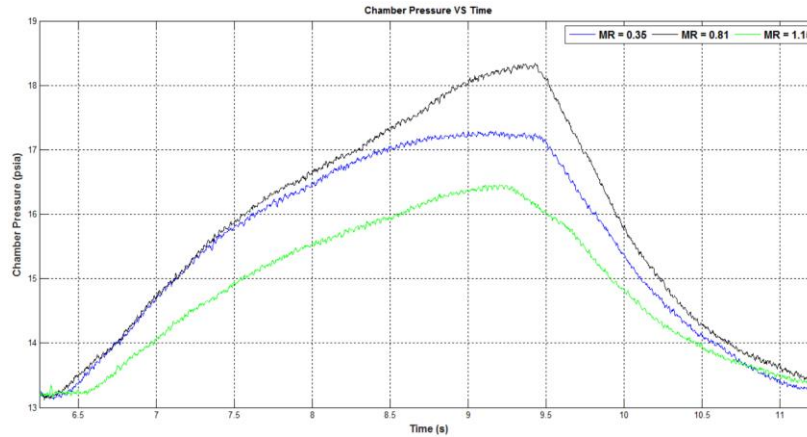


Figure 8.21 Liquid/liquid hot fire tests chamber pressure results

Since it was seen again that the chamber pressures were lower than expected a predicted approach was taken to try and understand what chamber pressures should have been enveloped within the engine during testing. RPA software was utilized to iterate through rocket engine design equations based on the inlet conditions of the test points (i.e. MR, inlet pressures, inlet temperatures) and the resulting flowrates. The following table shows the results of the analysis

Table 8.5: Predicted chamber pressures based on RPA software

Test ID	MR	Measured P_c (psia)	RPA Predicted P_c (psia)
1	0.35	17.3	17
2	0.81	18.3	36
3	1.15	16.5	42

The RPA software tool did indeed show that to produce the same amount of flowrates at the specified MR a higher chamber pressure would be needed. In the case of an MR of 0.35 it can be assumed that the P_c should be relatively low since the MR is low leading to predicted less combustion efficiency within the chamber. The hypotheses mentioned within the gas/gas section still stand with the primary assumption being the pressure port orifice being too small. A potential resolution could be to machine a bigger hole and also place the pressure port further upstream of the nozzle and evaluate the results thereafter.

Initial pops were noticed during testing, however these had no detrimental effect to the engine nor were they seen on the pressure traces of the chamber pressures. The plumes for all

tests were nominal with no significant effect of flow separation or underexpansion seen. The video images of each firing duration can be viewed in the following figure

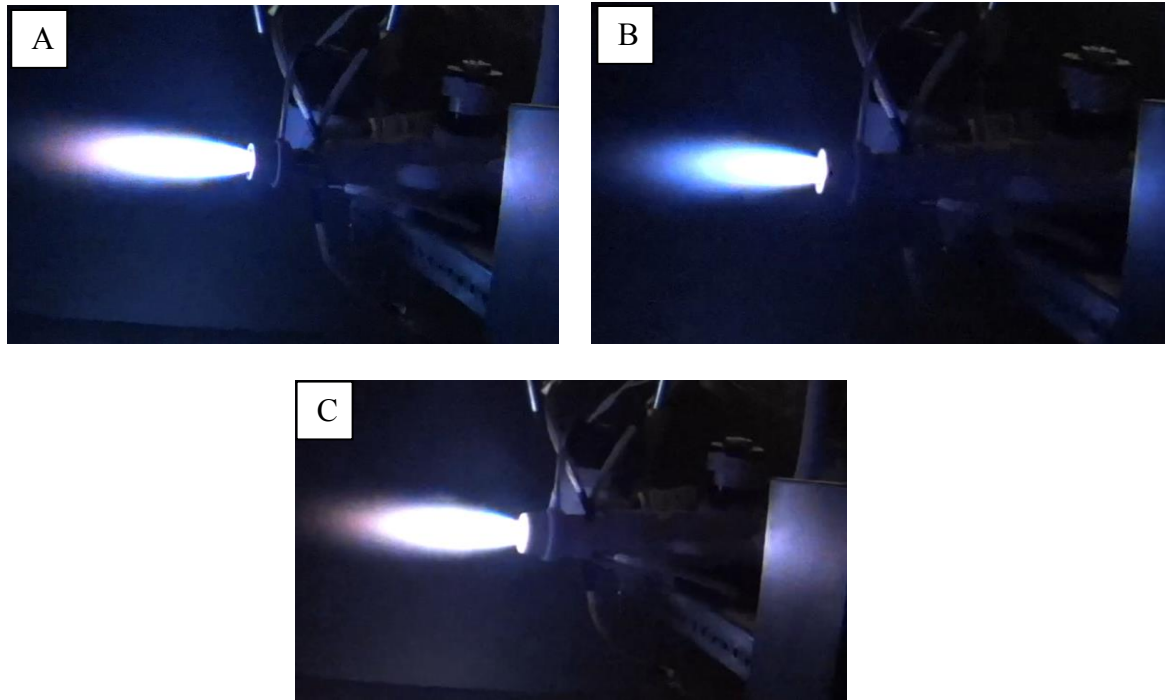


Figure 8.22 Video imaging of the liquid/liquid tests; A) $MR=0.35$, B) $MR=0.81$, C) $MR=1.15$

Chapter 9: Future Work and Conclusions

Future work for the RCS engine consists of first researching and fixing any potential issues associated with instrumentation on the engine. After this is complete then a detailed test matrix can be brought into the equation for which the engine will be tested. Due to the engines complex internal geometries additive manufacturing can also play a significant role moving forward.

9.1 Proposed Hot Fire Test Matrix

Since the engine will eventually be incorporated within two vehicles it is important to understand how the performance will measure up at various inlet conditions. For that reason a test matrix for liquid/liquid testing was developed which will look into varying the inlet pressures and also varying the film cooling percentages. The matrix is presented below in the following table

Table 9.1: Proposed test matrix for liquid/liquid testing

Oxygen (LOX)				Methane (LCH4)						MR		
Tank Pressure [psia]	Temp [F]	Density [lbm/ft^3]	Predicted mdot [lbm/s]	Tank Pressure [psia]	Temp [F]	Density [lbm/ft^3]	Predicted Combustion mdot [lbm/s]	FFC±5 %	Predicted Total Flow [lbm/s]	Predicted Combustion MR	Predicted Overall MR	
180	-296	71.171	0.037	140	-257	26.333	0.015	0	0.015	2.46	2.46	
								15	0.018		2.09	
								30	0.021		1.72	
				130		26.329	0.013	0	0.013	2.84	2.84	
								15	0.015		2.42	
								30	0.019		1.99	
				120		26.325	0.011	0	0.011	3.48	3.48	
								15	0.012		2.96	
								30	0.015		2.44	
150	-296	71.142	0.029	140	-257	26.333	0.015	0	0.015	1.95	1.95	
								15	0.018		1.66	
								30	0.021		1.36	
				130		26.329	0.013	0	0.013	2.25	2.25	
								15	0.015		1.91	
								30	0.019		1.57	
				120		26.325	0.011	0	0.011	2.75	2.75	
								15	0.012		2.34	
								30	0.015		1.93	
120	-296	71.113	0.018	140	-257	26.333	0.015	0	0.015	1.23	1.23	
								15	0.018		1.05	
								30	0.021		0.86	
				130		26.329	0.013	0	0.013	1.42	1.42	
								15	0.015		1.21	
								30	0.019		1.00	
				120		26.325	0.011	0	0.011	1.74	1.74	
								15	0.012		1.48	
								30	0.015		1.22	

In table 9.1 the variable parameters are the inlet pressures and the FFC percentages which are set by the needle valve. A MR range of 1-3.5 was chosen since initial engine design predictions saw these numbers as the upper and lower boundaries of the Isp curve. Also FFC percentages would vary between 0 to 30% in order to validate whether FFC will have any significant impact on delivered thrust. Lastly, the engine chamber was designed to be machined off reconfigured back onto the thruster in order to shorten the chamber length. Once testing for an L^* of 12 in is complete, shortening the chamber length to 10 in can commence and the proposed test matrix can be evaluated at this point as well. Comparing the results from the chamber length at $L^*=12$ in to $L^*=10$ in will give insight into whether the chamber is longer than it needs to be. From these results the flight engine envelope and design can begin to take shape.

9.2 Potential Incorporation of Additive Manufacturing

Additive manufacturing, or 3D printing, can be a potential alternative manufacturing method moving forward with the RCE. For that reason, an initial 3D printed prototype of the RCE was developed at the W.M. Keck Center at UTEP. A major goal of printing the RCE, and any other component, is to have a functional part that performs the same way as conventional machined parts; therefore, an initial nondestructive test was performed to try and understand the performance of the 3D printed engine compared to the conventionally machined engine.

The RCE was printed by using selective laser melting (SLM) technology in which metal powders are melted onto each other and bonded, layer by layer, to form 3D components. Figure 9.1 below gives a brief description of the process associated with SLM¹⁵

¹⁵ (Bremen, 2012)

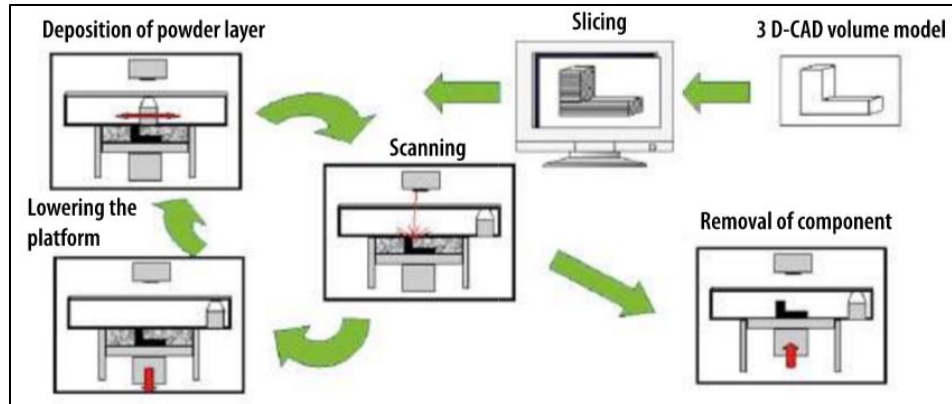


Figure 9.1 SLM manufacturing process, starting from the top right

As seen from figure 1, first a computer aided design (CAD) model of the RCE was generated and formatted such that it would comply with the software used for the SLM machines. This design was similar to the conventional machined RCE assembly except for some minor modifications to help with the additive manufacturing process. Then the SLM machine was loaded with Inconel 625 powder for which the engine would be made from. Afterwards, the machine used a laser to melt the powder and form layer by layer the RCE. This was accomplished by melting a layer of the part and then, the machine automatically, lowering the build platform. To conclude, once complete the part was removed from the machine and cleaned for future post machining processing.

The engine shown below in figure 9.2 is the final product of the 3D printed engine with post machining already performed and the tubing inlets welded on

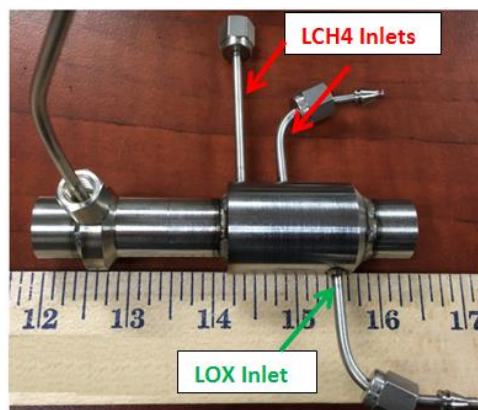


Figure 9.2 Post machined 3D printed engine

As can be seen from figure 9.2 the engine was polished on the exterior in order to apply a smooth roughness finish. However, internally the engine's surface still remained course due to the fact that the engine was printed meaning significant alignment of powdered particles on the top surface would be highly difficult. Figure 9.3 shows the internal surfaces of the engine looking from the top and bottom views

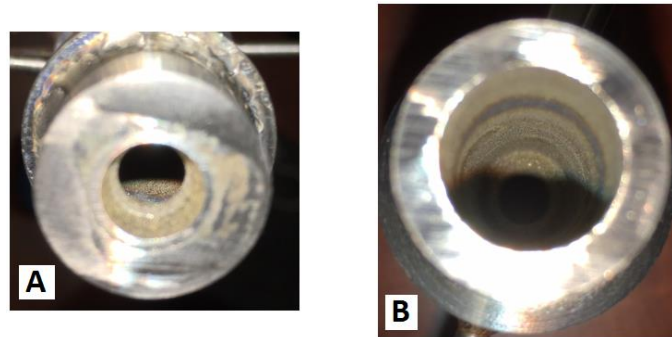


Figure 9.3 Nozzle view (A) and the igniter view (B)

In order to have a better understanding of the internal geometry of the engine, mainly the injector, injector water tests were performed to see how the injector would compare to predicted data and the RCE which was conventionally machined. The same water test set-up which was used for the conventionally machined engine was used for the 3D printed engine. Due to difficulties with the LCH4 line the data which is presented within this section will primarily cover the oxygen line. The table below shows the test results from water tests

Table 9.2: Test matrix and results of water testing the LOX injection ports

<i>Oxygen Line Test Matrix</i>								
Test Run	Tank Pressure PT-1 [PSIG]	Injector ΔP (PT2 - PT5) [PSIG]	Measured \dot{m} [lbm/s]	Predicted \dot{m} [lbm/s]	% Difference	Measured Cd	\dot{m} (using ρ_{LOX} and Cd = 0.65) [lbm/s]	\dot{m} (using ρ_{LOX} and measured Cd) [lbm/s]
1	20±2	21.7	0.007	0.015	53%	0.28	0.016	0.008
2	40±2	40.6	0.010	0.021	52%	0.30	0.023	0.011
3	60±2	61.0	0.012	0.026	54%	0.31	0.028	0.013
4	80±2	81.0	0.015	0.030	50%	0.32	0.032	0.015
5	80±2	81.6	0.015	0.030	50%	0.32	0.032	0.015
6	60±2	61.2	0.013	0.026	50%	0.32	0.028	0.013
7	40±2	41.1	0.010	0.021	52%	0.31	0.023	0.011
8	20±2	21.4	0.007	0.015	53%	0.31	0.016	0.008
9	20±2	21.7	0.007	0.015	53%	0.31	0.016	0.008
10	40±2	41.0	0.010	0.021	52%	0.32	0.023	0.011
11	60±2	61.2	0.013	0.026	50%	0.32	0.028	0.013
12	80±2	81.1	0.015	0.030	50%	0.32	0.032	0.015
					Average	0.31	% Difference	50.0%

The predicted data used a discharge coefficient value of 0.65 which was considered to be a conservative number. However what was seen from testing was the discharge coefficient ended up being half of that value which in turn generated flow rates significantly lower than the predicted. After correlating the flowrates of water to the flow rates that would be seen with LOX the data displayed the same trend in that the predicted values were close to two times the amount of the measured values. As a result, the overall percent error that was determined from the tests was ~50%. When the pressure drops vs the mass flow rates were plotted against each other the following graph in figure 9.4 was generated

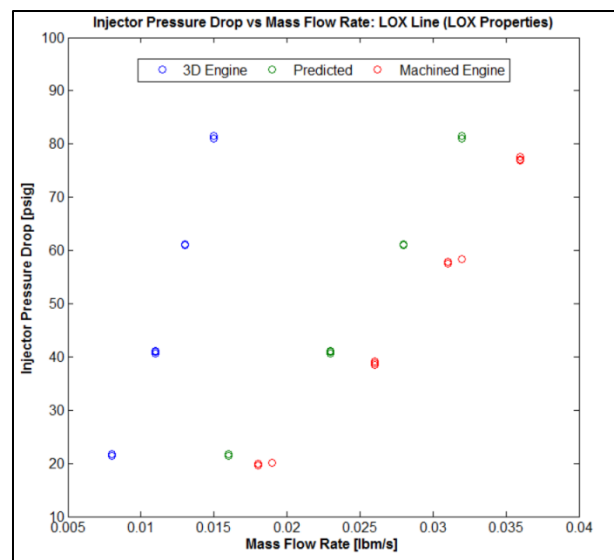


Figure 9.4 LOX line pressure drop vs mass flow rate correlation

It can be clearly seen in figure 9.4 that the pressure drop is significantly higher than the predicted values or the tested values from the conventionally machined engine. This can be attributed to potential blockage within the manifolds, or the injection orifice sizes not being properly made. Overall the 3D printed engine did not perform as predicted, but progress was made in understanding the future steps necessary to have a full functioning part. Initial water tests assisted in determining starting points for potential investigations of the engine such as the orifice sizes and the internal geometries of the propellant manifolds. Future studies will consist of machining a cross section of the engine and inspecting the injection orifice sizes along with

the internal features of the manifolds. Once inspections are complete the redesign of the engine can take place and various assembly and print methods can be discussed.

9.3 Overall Conclusions

The reaction control engine was designed to be tested for multiple scenarios that a flight engine might see. In performing initial cold flow and hot fire tests with the engine what was seen was lower performance in the hot fire tests than predicted. This is not necessarily attributed to the engine itself, but instead can be a function of the test set-up. Certain items such as flex hoses on the hot fire test set-up can be re-evaluated if need be in order to allow for a more accurate form of thrust measurement. Also, potential modification to the engine pressure port would allow for future researchers to determine whether or not the chamber pressure is within the vicinity or higher than what was measured with the current tests. With these potential changes, a proposed liquid/liquid test matrix, and potential incorporation of rapid prototyping through additive manufacturing means the engine could go into a rigorous test campaign which would output a significant amount of valuable data dealing with LOX/LCH₄ propulsion.

Bibliography

- [1] Siceloff, S. (2014, April 23). *Equipped with New Sensors, Morpheus Preps to Tackle Landing on its Own*. Retrieved August 15, 2016, from NASA.gov:
<https://www.nasa.gov/content/equipped-with-new-sensors-morpheus-preps-to-tackle-landing-on-its-own/#.V8c6A5grKhd>
- [2] Hurlbert, E., Mcmanamen, J. P., Sooknanen, J., & Studak, J. W. (n.d.). *Advanced Development of a Compact 5-15 lbf LOX/Methane Thruster for an Integrated Reaction Control and Main Engine Propulsion System*. Houston, Texas 77058: NASA Johnson Space Center.
- [3] Hurlbert, E., Romig, K., Collins, J., Allred, J., & Mahoney, J. (2010). *Test Report for 870-lbf Reaction Control System Tests Using Liquid Oxygen/Ethanol and Liquid Oxygen/Methane at White Sands Test Facility*. Hanover: NASA Center for Aerospace Information.
- [4] Lopez, I. (2016). *Janus: LOX/LCH₄ Robotic Lander Testbed*. El Paso: Southwest Emerging Technology Symposium.
- [5] Klen, M. D. (n.d.). *Liquid Oxygen/Liquid Methane Propulsion and Cryogenic Advanced Development*. Cleveland: NASA Glenn Research Center.
- [6] *NASA Sounding Rockets User Handbook*. (2015). Wallops: NASA Goddard Space Flight Center.
- [7] Ponomarenko, A. (2015, October 6). *Rocket Propulsion Analysis*. Retrieved January 1, 2016, from <http://propulsion-analysis.com/index.htm>
- [8] Brown, C. (1996). *Spacecraft Propulsion*. Washington,DC: AIAA.
- [9] *Inconel alloy 718*. (2007, September 7). Retrieved January 1, 2016, from Special Metals:
<http://www.specialmetals.com/documents/Inconel%20alloy%20718.pdf>
- [10] Huzel, D. K., & Huang, D. H. (1992). *Modern Engineering for Design of Liquid-Propellant Rocket Engines*. Washington DC.: AIAA.
- [11] Huzel, D. K., & Huang, D. H. (1967). *Design of Liquid Propellant Rocket Engines*. Washington, D.C.: NASA.
- [12] Cengel, Y. A., & Cimbala, J. M. (2006). *Fluid Mechanics Fundamentals and Applications*. New York: McGraw-Hill.
- [13] Acosta-Zamora, A. (2012). *An Experimental Investigation on LOX/LCH₄ Reaction Control Thrusters*. El Paso: UTEP.

- [14] Mena, J. L. (2014). *Performance Evaluation of a LOX-LCH₄ Reaction Control System Thruster*. El Paso: UTEP.
- [15] Bremen, S. a. (2012). Selective Laser Melting. *Laser Technik Journal*, 33-38.

Appendix

Janus prototype test campaign:

Prototype	Characteristics	Purpose	Testing Capabilities
J-1	<ul style="list-style-type: none"> • Static test bed • Flexible interface for main engine and RCS 	<ul style="list-style-type: none"> • Test propulsion system • Demonstrate structural integrity of thrust mount & gimbal • Develop procedures, protocols, manufacturing techniques, DAQ & controls • Train personnel for vehicle test/flight operations 	<ul style="list-style-type: none"> • Main Engine/RCS integration • Tank Integration • Data Acquisition • Structural (Thrust Mount and Gimbal) • Actuation (Gimbal and Valve) • Tank Boil-off • Mission duty cycle
J-2	<ul style="list-style-type: none"> • Flight test bed • Non-autonomous (Tethered) 	<ul style="list-style-type: none"> • Develop flight hardware. • Create flight envelope & component package • Demonstrate vehicle dynamic integrity • Show telemetry capability • Implement A.M. Components • Possibly test composite tank 	<ul style="list-style-type: none"> • Same as Prototype 1 • Landing gear reliability • Telemetry/Communications • Limited GNC • Flight Monitoring Instruments
J-3	<ul style="list-style-type: none"> • Flight test bed • Autonomous(Non-tethered) 	<ul style="list-style-type: none"> • Demonstrate autonomous GNC integration • Employ SOFC power supply 	<ul style="list-style-type: none"> • Same as Prototype 2 • SOFC Power delivery (Non-flight first) • Autonomous GNC control

Daedalus prototype test campaign:

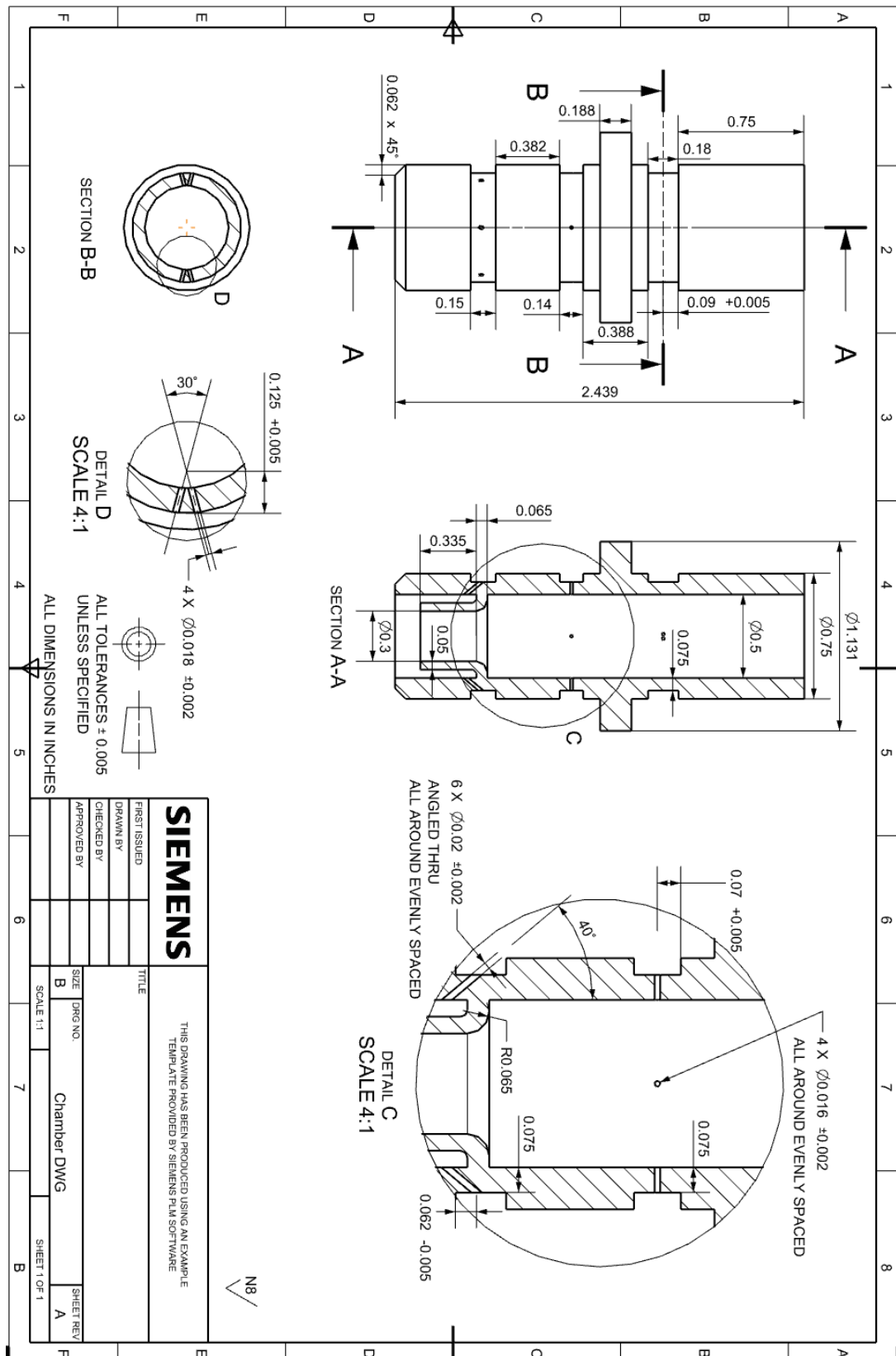
Prototype	Characteristics	Purpose	Testing Capabilities
D-1	Static test bed Flexible interface for main engine and RCS options	Test propulsion system Demonstrate structural reliability of vehicle	Main Engine/RCS integration Tank Integration Data Acquisition Structural (Vehicle) Actuation (Valves) Tank Boil-off Mission duty cycle
D-2	Flight test bed (Static)	Develop flight hardware Create flight envelope & component package Demonstrate vehicle dynamic integrity Show telemetry capability Implement A.M. Components Optimize weight for flight	Same as Prototype 1 Telemetry/Communications and Avionics Flight Monitoring Instruments
D-3	Autonomous suborbital flight	Demonstrate autonomous GNC integration Demonstrate LOX/LCH ₄ engine performance under micro gravity conditions	Main Engine/RCS integration Telemetry/ Communications and Avionics Flight Monitoring Instruments

RCE design requirements:

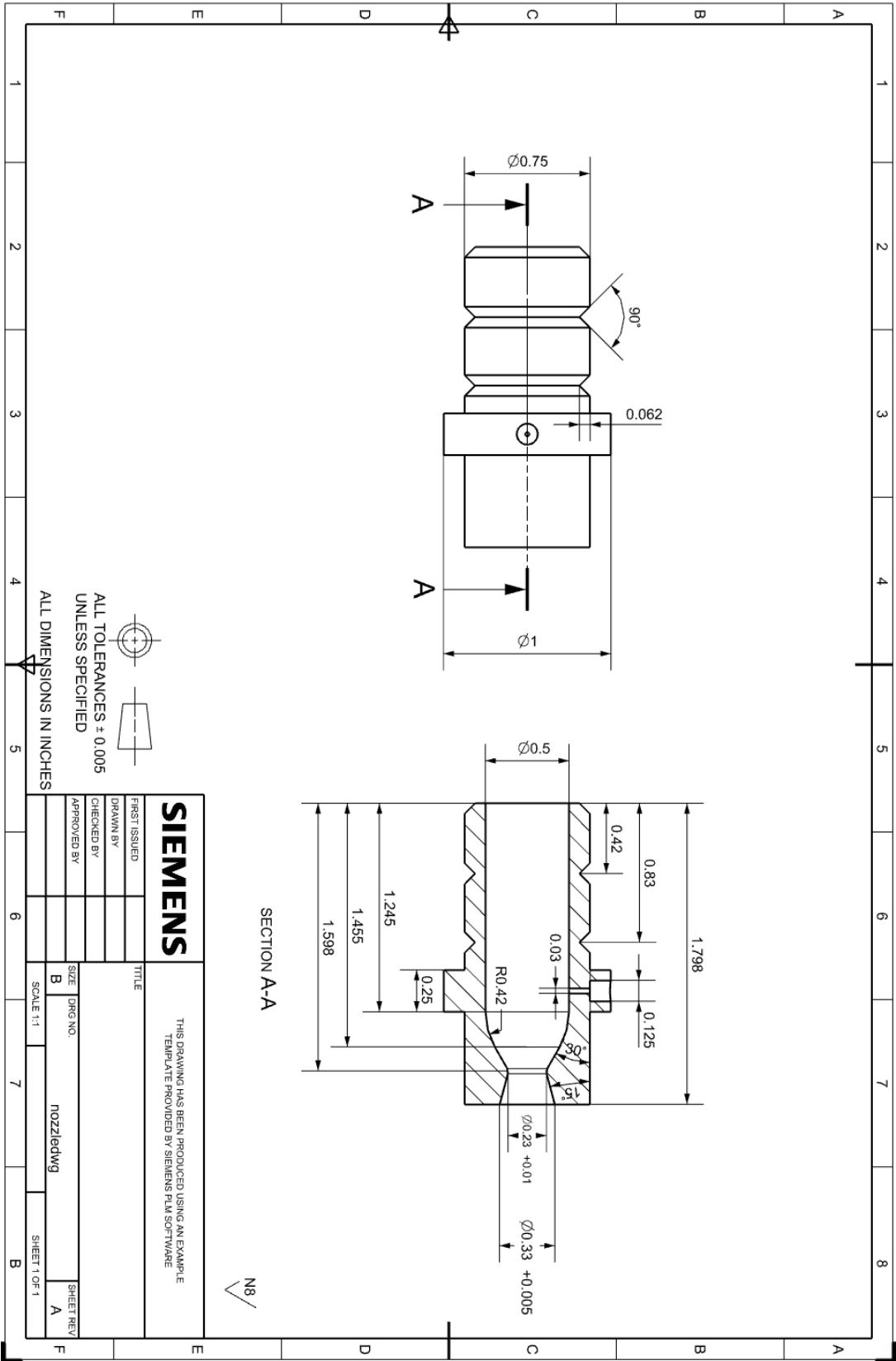
RCE Design Requirements

Engine Parameters:		Engine Mass Estimate and Envelope:	
Thrust		Max Engine Mass	3.3 lbm
Janus	5 lbf	Engine Envelope	
Daedalus	7 lbf	Diameter	TBD in
Specific Impulse		Length	TBD in
Janus	182 s	F/W Ratio	
Daedalus	255 s	Janus	1.5
Mixture Ratio	1.54 O/F	Daedalus	2.4
Film Cooling %	30 %	Oxidizer Side (Pressurized by Helium):	
Oxidizer Conditions (LOX):		Injector Pressure Drop	20 psia
Temperature	-296 °F	Solenoid Valve Pressure Drop	1 psia
Pressure	120 psia	Line Orifice Pressure Drop (single)	TBD psia
Density	71.24 lbm/ft ³	Required Line Pressure Drop	
Flow Rate	0.01665 lbm/s	Janus	230 psia
Fuel Conditions (LCH ₄):		Daedalus	230 psia
Temperature	-257 °F	Oxidizer Tank Pressure	
Pressure	120 psia	Janus	350 psia
Density	26.36 lbm/ft ³	Daedalus	350 psia
Flow Rate (Combustion)	0.00833 lbm/s	Fuel Side (Pressurized by Helium):	
Flow Rate (Film Cooling)	0.00250 lbm/s	Injector Pressure Drop	20 psia
Thrust Chamber:		Solenoid Valve Pressure Drop	1 psia
Chamber Pressure	100 psia	Line Orifice Pressure Drop (single)	TBD psia
C* Efficiency	92 %	Required Line Pressure Drop	
C*	5302 ft/s	Janus	230 psia
Cf Efficiency		Daedalus	230 psia
Janus	95 %	Fuel Tank Pressure	
Daedalus	97 %	Janus	350 psia
Cf		Daedalus	350 psia
Janus	1.15		
Daedalus	1.71		
Contraction Ratio	5		
Expansion Ratio			
Janus	2		
Daedalus	40		
Throat Area A _t	0.043 in ²		
Throat Diameter D _t	0.23 in		
L*	12 in		
Nozzle Contour			
Janus	15° Conical		
Daedalus	78% Bell		

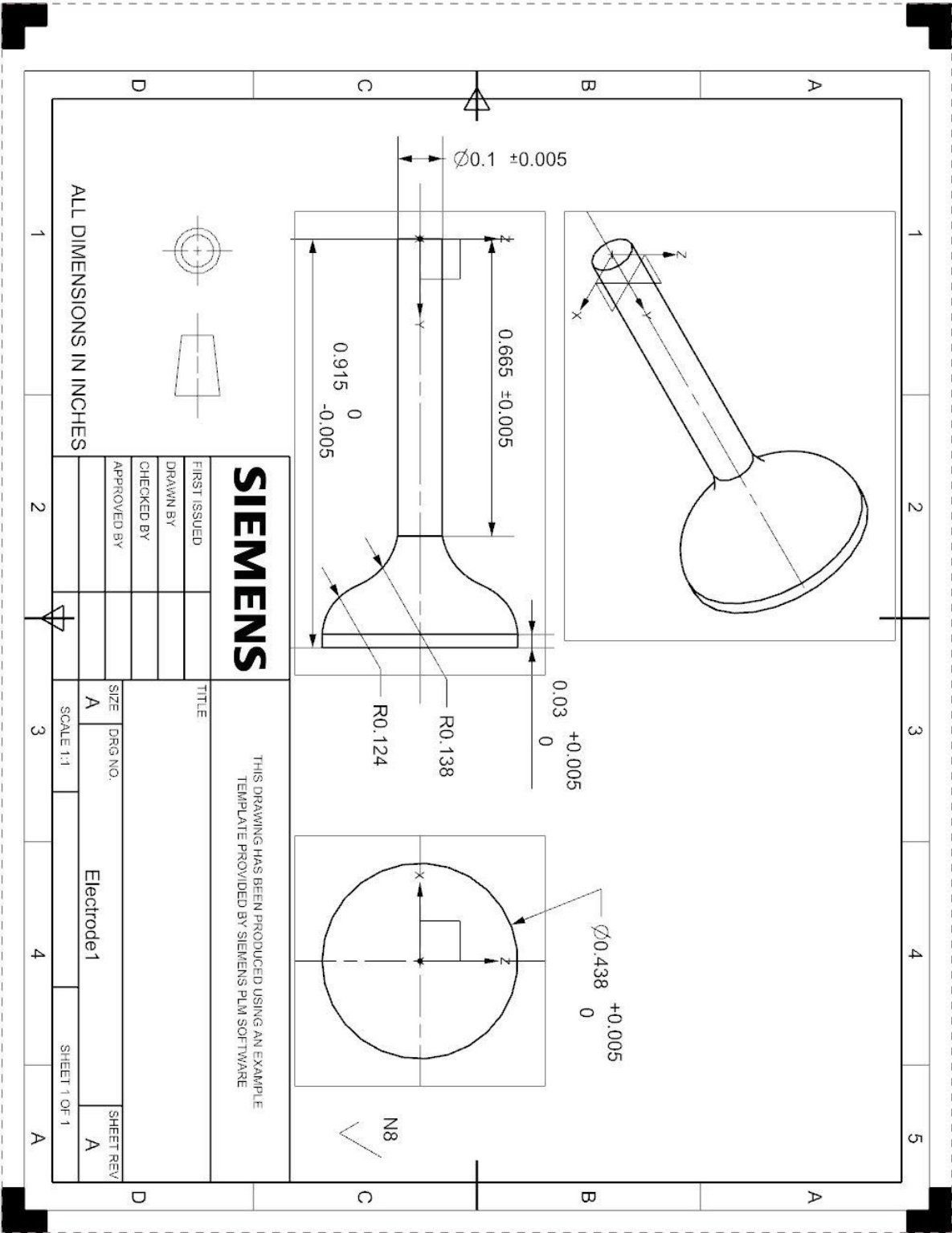
RCE chamber drawing:



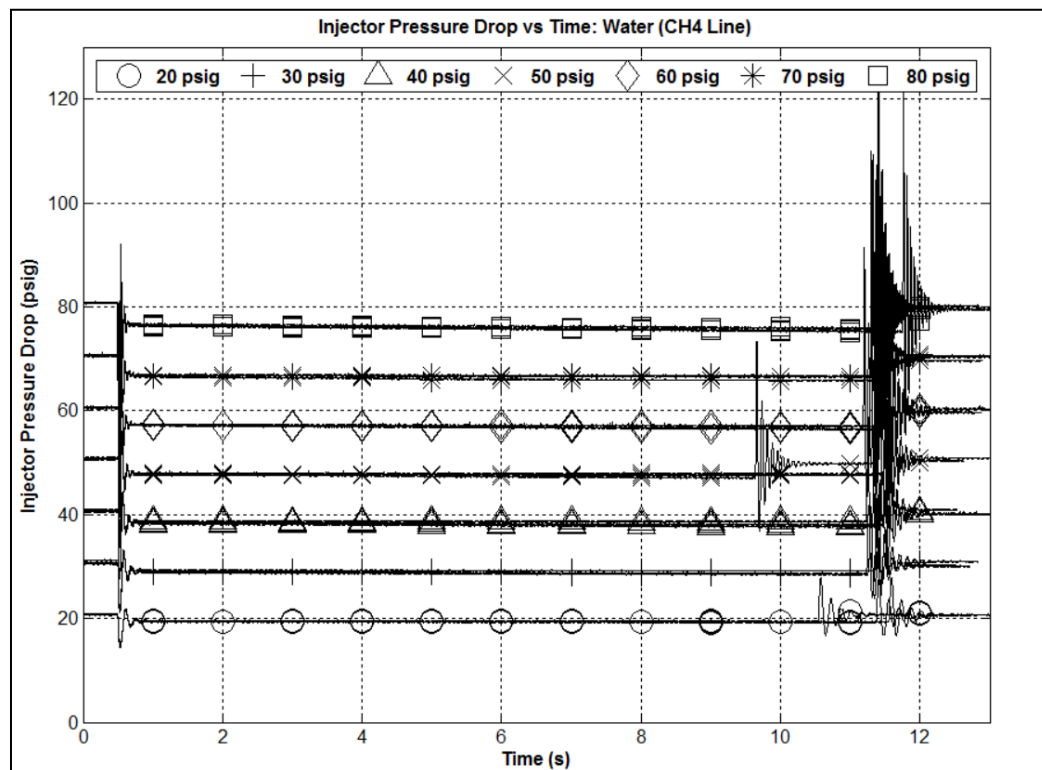
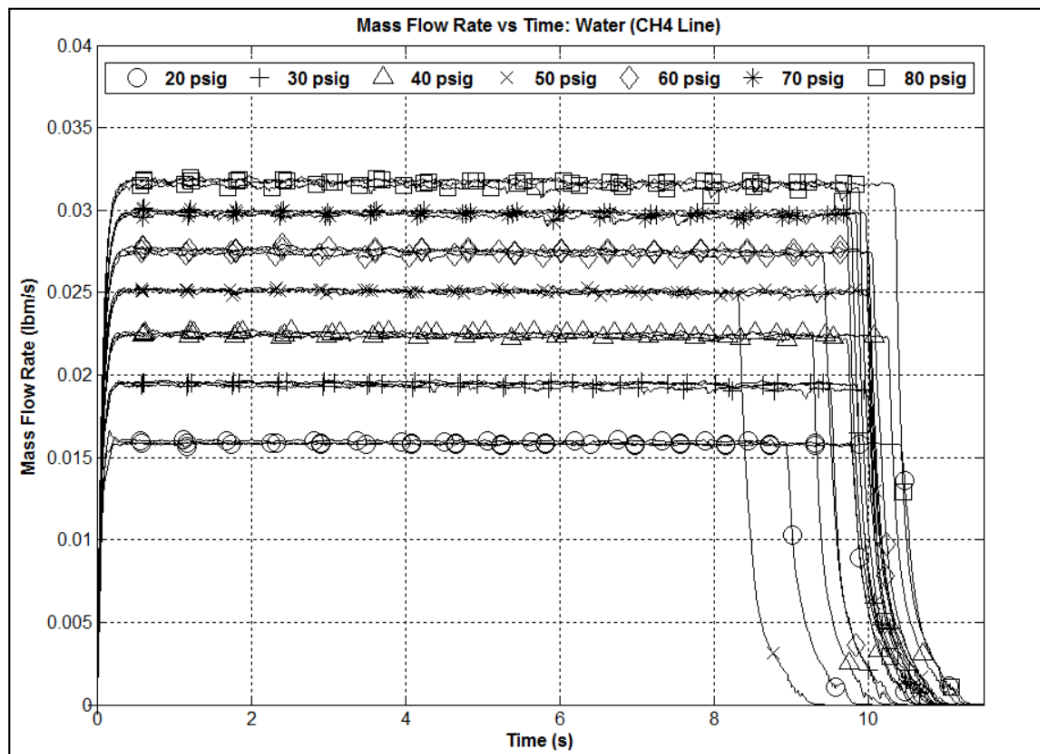
RCE nozzle drawing:



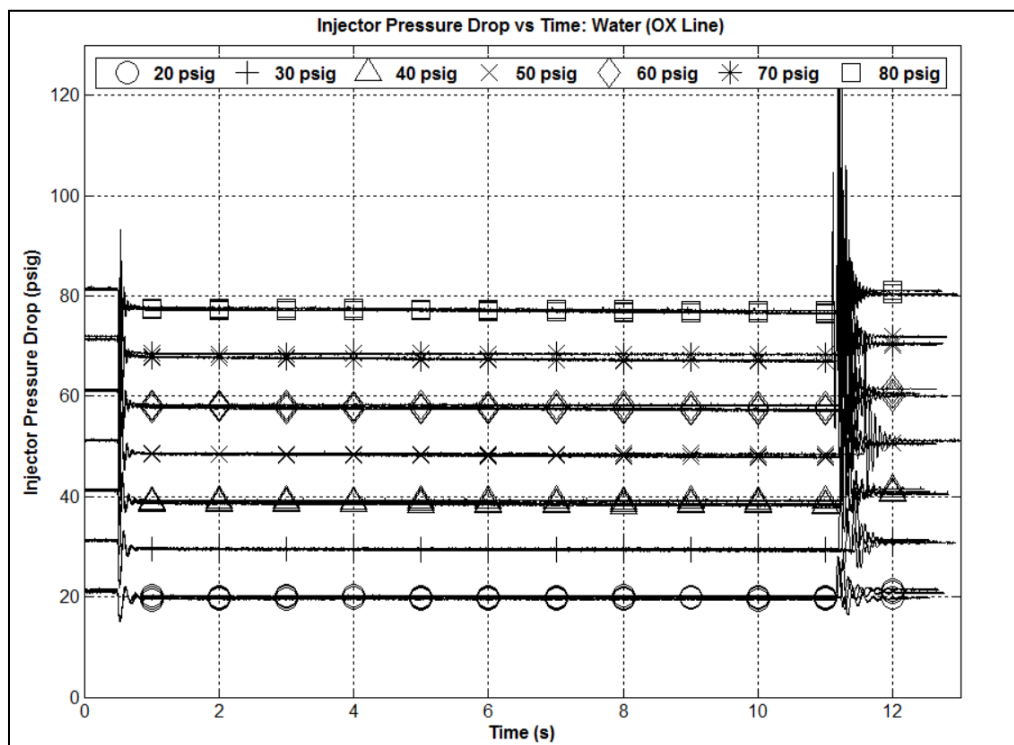
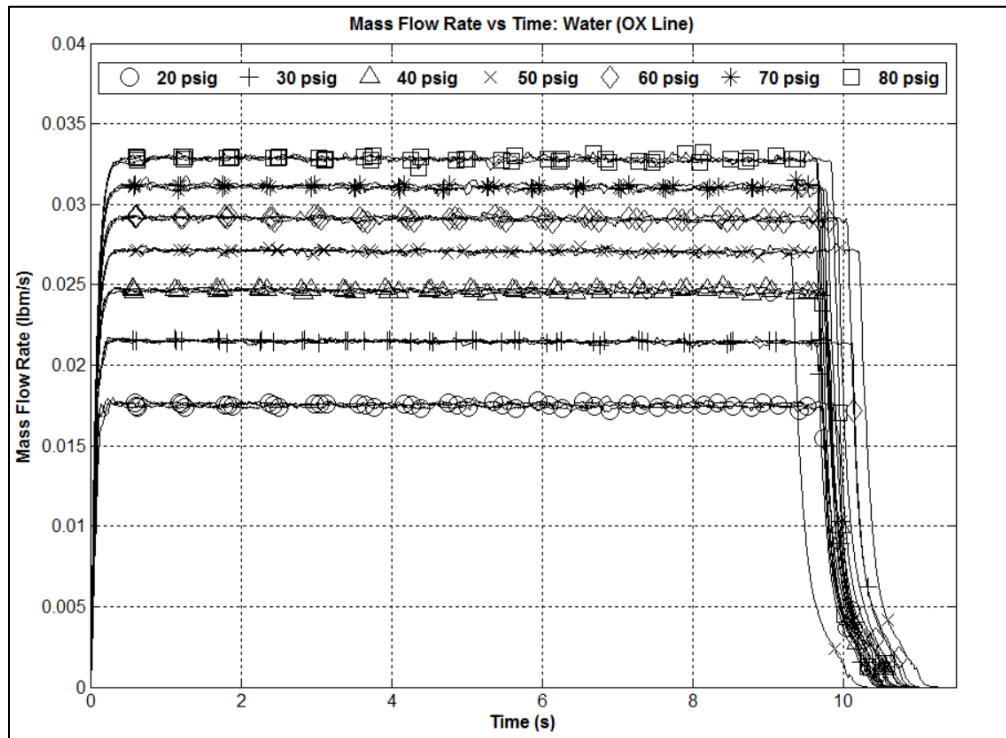
RCE igniter electrode drawing:



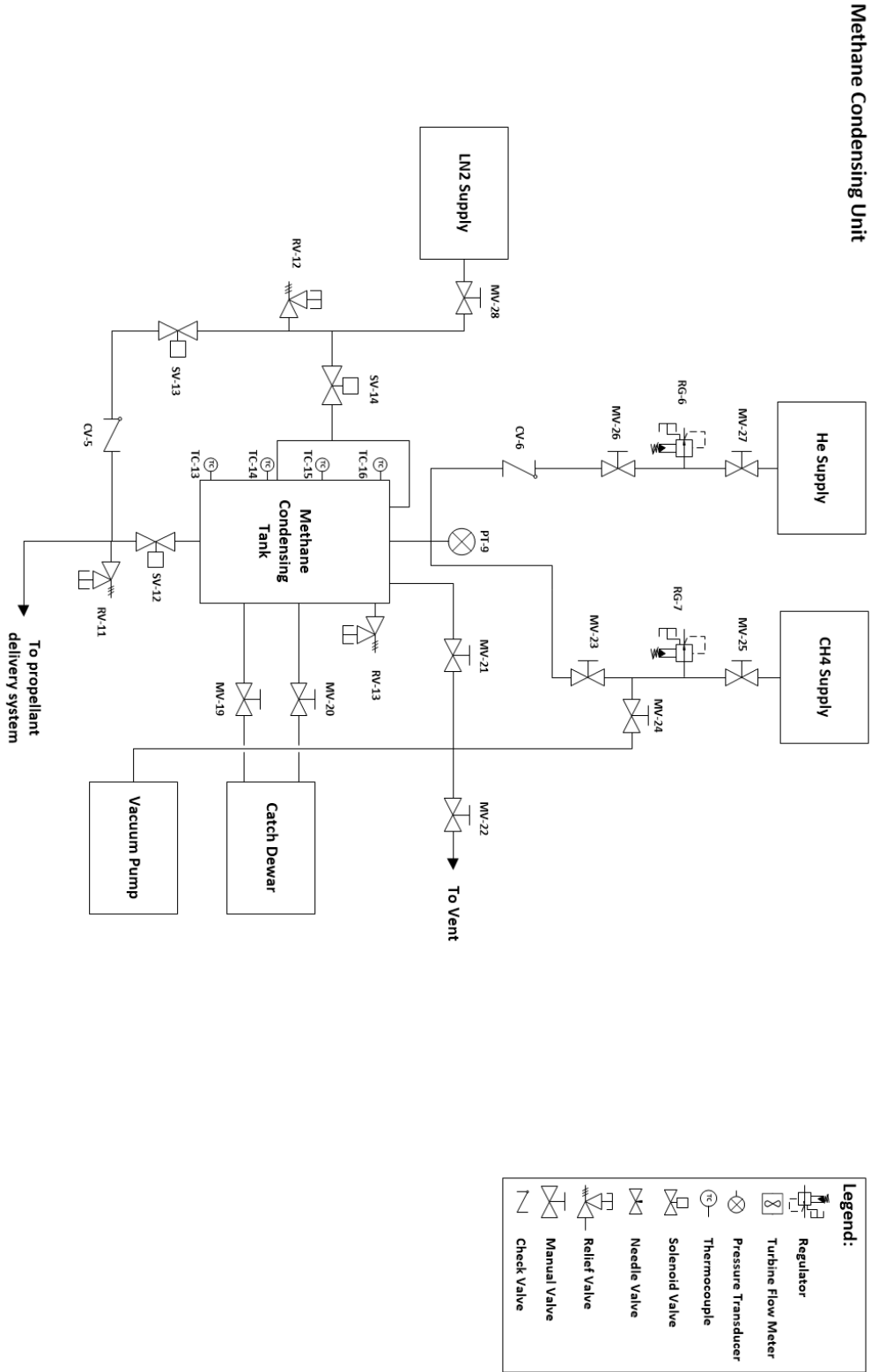
LCH4 line raw water test data:



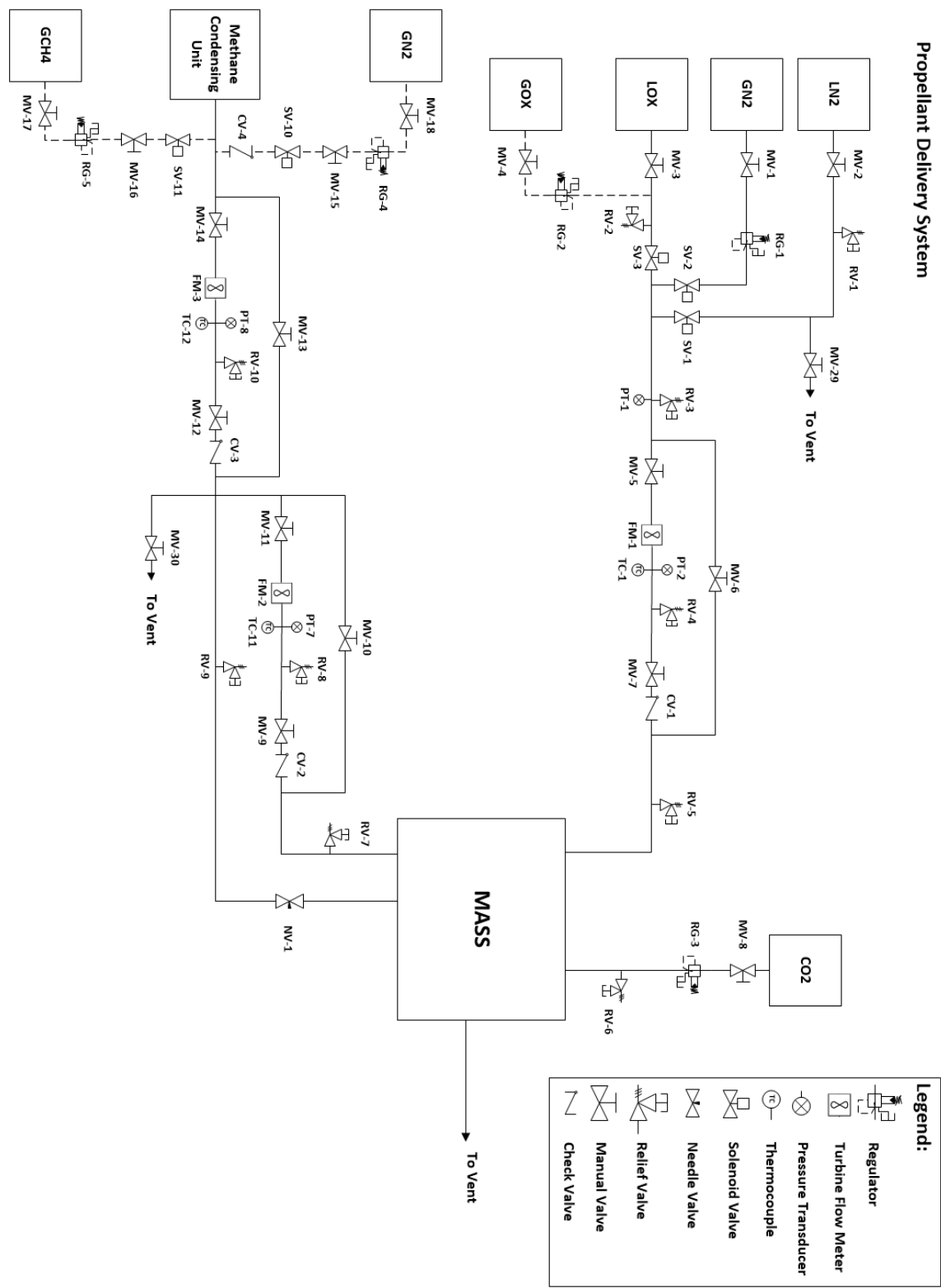
LOX line raw water test data:



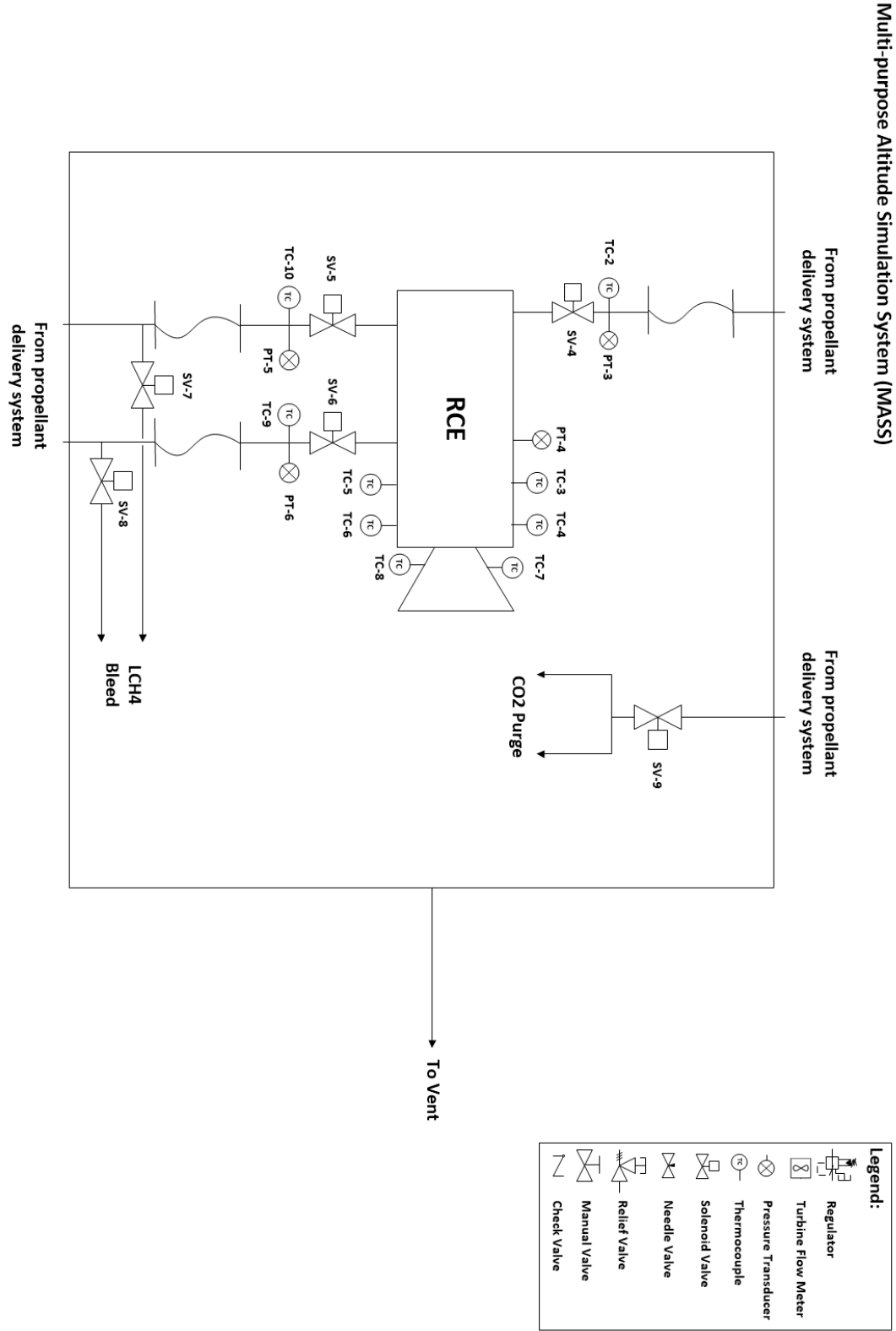
Methane condensing unit P&ID:



Bunker propellant delivery system P&ID:



Components within the MASS P&ID:



Vita

Aaron Johnson attained his Bachelors of Science degree in Mechanical Engineering from the University of Texas at El Paso in the spring of 2014. He continued his undergraduate research pertaining to LOX/LCH₄ rocket engines at the center for space exploration and technology research (cSETR) lab by pursuing a Master's of Science in Mechanical Engineering at UTEP. Before his final year as a graduate student he completed an internship at Orbital ATK for which he worked within the propulsion group performing analyses on rocket motors.

Before graduation Aaron Johnson accepted an offer to work with Blue Origin as a propulsion development engineer, and is currently working with the company out in their West Texas facility.

Permanent address: 1739 Onizuka Dr.

El Paso, TX, 79936

This thesis was typed by Aaron Johnson.